Geoscience Letters

RESEARCH LETTER

Open Access

Sedimentary evolution pattern influenced by sequence stratigraphy: a case study of the Nanpu Sag, Bohai Bay Basin, China

Zhongqiang Sun[1*], Shuangyue Lin[1], Guangqun Wang[2], Longlong Liu[1] and Mengqi Wang[3]

Abstract

Identifying and characterizing sedimentary evolution patterns are crucial for assessing the distributions of source and reservoir rocks, which are fundamental to hydrocarbon exploration. This study analyzed the stratigraphic sequence, lithological characteristics, sedimentary lithofacies, individual well sedimentary sequences, and seismic reflection properties. The analysis revealed six fourth-order sequences, including progradational and regressive sequences, indicative of water level changes. The sediment sources for the second and third sub-members of the Eocene Shahejie Formation's third member (Es_3^{2+3}) in the Nanpu Sag were identified as the Baigezhuang and Xinanzhuang Uplifts. Predominantly, the sandstones are lithic arkose and feldspathic litharenite, both of which exhibit low compositional and structural maturity. Notably, 22 lithofacies and 8 lithofacies associations suggest fan delta processes. This study identified three fundamental seismic reflection package reflection types. These lithofacies associations, sedimentary sequences, and seismic reflections serve as critical indicators for determining sedimentary environments. The results from the sedimentary facies analysis indicate that the Es_3^{2+3} Formation developed fan delta deposits, controlled by the sequence of the sedimentary evolution pattern. The potential of these fan delta sediments to form oil and gas reservoirs is significant. Therefore, precise characterization of the sedimentary evolution pattern is essential for a comprehensive understanding of basin dynamics and hydrocarbon potential.

Keywords Nanpu Sag, Shahejie Formation, Fan delta, Sequence stratigraphy, Sedimentary evolution pattern

Introduction

The evolution of sedimentary patterns for fan deltas has long been a focal point of geological research due to its implications for hydrocarbon exploration (Kang et al. 2019; Mahata and Maiti 2019; Moore et al. 2020). Geologists have extensively studied the origins, transport mechanisms, and distribution patterns of sediments, particularly focusing on how stratigraphic sequences influence fan delta evolution (Liu et al. 2020; Moran et al. 2023; Yang et al. 2023). Understanding fan delta evolution processes influenced by stratigraphic sequences is crucial for accurately locating oil and gas reservoirs (Sun et al. 2023a).

The relationships among the formation, and evolution of fan deltas, and stratigraphic sequences continue to be a significant subject in geological studies (Feng et al. 2021; Xu et al. 2023a). Recent advancements in science and technology have led to substantial progress in this area, particularly through the development of various stratigraphic sequence patterns. These patterns are invaluable tools for analyzing the depositional processes and spatiotemporal distribution of fan delta systems (Catuneanu 2006; Allen

*Correspondence:
Zhongqiang Sun
sunzhongqiang@lingnan.edu.cn
[1] School of Geographical Science, Lingnan Normal University, Zhanjiang 524048, China
[2] China Construction Fifth Engineering Division Corp., Ltd, Changsha 410000, China
[3] School of Geography and Environment, Liaocheng University, Liaocheng 252000, China

and Fielding 2007a, 2007b; Boggs 2011). Researchers have compared stratigraphic interfaces to establish isochronous frameworks, facilitating detailed analyses of fan delta configurations within these sequences (Allen and Fielding 2007a). Such studies elucidate the spatial distribution, morphological characteristics, and sedimentary environments of fan delta deposits, providing essential data for further stratigraphic sequence comparisons and classifications.

Research on the relationships between fan delta system evolution and stratigraphic sequences has increasingly embraced interdisciplinary methods. Techniques such as three-dimensional computer modeling, geophysics, geochemistry, and paleontology provide comprehensive technical and theoretical support for these studies. However, challenges persist in fully understanding this relationship (Peter 2016). The formation and evolution of strata are dynamic processes influenced by various factors including tectonic activities, climate changes, and water-level fluctuations. These elements collectively determine the morphology, structure, and composition of strata (Hunt and Tucker 1992; Miller et al. 2005; Haq and Schutter 2008). Researchers have examined rock types, fossil assemblages, and mineral compositions to elucidate sedimentary environments and formation processes (Rohais et al. 2008; Kalifi et al. 2020). Additionally, the depositional processes of fan delta system are influenced by tectonic subsidence, relative water-level changes, and fault movements, all of which require further detailed investigation (Rohais et al. 2008; Kalifi et al. 2020). In essence, the intricate relationship between fan delta system evolution and stratigraphic sequences warrants more extensive exploration.

This paper focuses on the Shahejie Formation in the Nanpu Sag, Bohai Bay Basin, and explores the sedimentary patterns and the impact of stratigraphic sequences on the evolution of fan deltas. The Bohai Bay Basin, known for its extensive oil and gas fields, showcases the high potential of the Shahejie Formation for hydrocarbon extraction (Liu et al. 2016; Li et al. 2018; Tang et al. 2019; Sun et al. 2021). The identification of sedimentary evolution patterns within this context is pivotal in pinpointing potential sources and reservoir rocks. Recent studies have highlighted the need for patterns that incorporate key influencing factors such as tectonic subsidence, sediment supply, eustacy, and climate to comprehensively understand the evolution processes of the fan delta system in the Nanpu Sag, thus guiding the effective use of cores, wireline logs, seismic data, and SEM analyses in establishing sequence-controlled sedimentary patterns (Li et al. 2018; Liu et al. 2019).

Geological setting and stratigraphy

Geological setting

The Bohai Bay Basin, which is located in northern China, is flanked by the Jiaoliao Uplift to the east, the Taihang Mountain Uplift to the west, the Dongpu Depression to the south, and the Yanshan Uplift to the north. This Mesozoic–Cenozoic fault basin evolved during the Indosinian and Yanshanian movements, following the Paleozoic sedimentation of the Sino-Korean paraplatform (Liu et al. 2016; Sun et al. 2021). It is the primary region of offshore oil and gas fields in China, with significant deposits located in the Huang Depression, Liaohe Depression, Jizhong Depression, Jiyang Depression, Dongpu Depression, Linqing Depression, and Chengning Uplift (Liu et al. 2023; Pang et al. 2023; Fig. 1a, b).

To the north of the Huanghua Depression lies the Nanpu Sag, a Mesozoic–Cenozoic sag that is part of the oil and gas-rich Bohai Bay Basin area, surrounding the Bohai Sea (Liu et al. 2023; Pang et al. 2023). Defined by the Baigezhuang Fault to the northeast, the Xinanzhuang Fault to the southwest, and the Shabei Fault to the south, the sag is segmented into six sub-sags (Liu et al. 2023; Pang et al. 2023; Sun et al. 2023b; Fig. 1c). The northern boundary of the Shichang sub-sag is marked by the Baigezhuang Fault, abutting the Baigezhuang and Matouying Uplifts, while the northwestern border is defined by the Xinanzhuang Fault and the southern boundary coincides with the Shaleitian Uplift at the Gaoliu Fault (Liu et al. 2023; Pang et al. 2023; Sun et al. 2023b; Fig. 1d). This typical fault basin, developed atop the North China Platform's basement, is characterized by the Gaoshangpu oilfield within the Gaoliu structural belt. Dominated by multilevel fault blocks such as G14, G5, G11, and G66, this structural-lithologic reservoir, buried between 2900 and 4600 m, possesses considerable exploration and development potential.

The formation and internal structural style of the Nanpu Sag were influenced by various factors, including tectonism, provenance, and climate, with tectonism playing a predominant role. The Paleogene structural evolution of the Nanpu Sag is characterized by four distinct rifting stages:

(1) *Stage I.* Corresponding to the Es_3^{4+5} sedimentation period, this initial stage marked the activation of the Baigezhuang and Xinanzhuang Faults. The basin evolved into a shallow half-graben depression, predominantly within the Shichang Depression, extending southwest (Wu et al. 2022; Sun et al. 2023b; Zou et al. 2023; Fig. 2).
(2) *Stage II.* During the Es_3^3 to Es2 sedimentation period, intense faulting occurred, positioning the sedimentary center north of the Gaoshangpu struc-

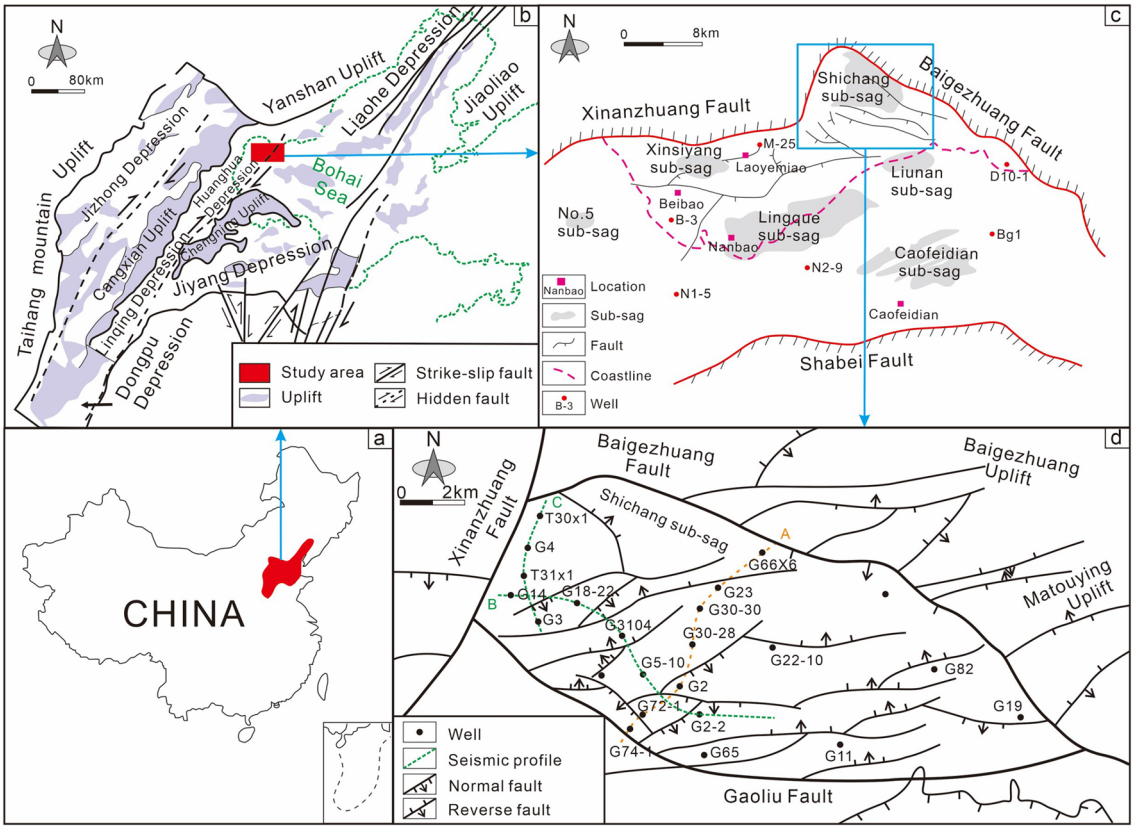

Fig. 1 **a** Location of the Bohai Bay Basin of China; **b** tectonic units of the Bohai Bay Basin; **c** tectonic units of the Nanpu Sag; **d** well locations and structural units of the study area

tural belt and west of the Liuzan structural belt. This period saw the proliferation of small fan delta systems comprising conglomerates, pebbly sandstones, and gray-green mudstones, forming the primary oil-bearing and reservoir sequences of the Paleogene in the Nanpu Sag (Wu et al. 2022; Pang et al. 2023; Sun et al. 2023b; Zou et al. 2023; Fig. 2).

(3) *Stage III*. Equivalent to the Es1 sedimentation period, this stage featured less intense rifting than Stage II, transitioning from an uplifted to a rifted state (Wu et al. 2022; Pang et al. 2023; Sun et al. 2023b; Zou et al. 2023). The sedimentary environment was dominated by shallow waters with significant hydrocarbon source rock development (Fig. 2).

(4) *Stage IV*. Aligning with the Dongying Formation period, this final stage experienced reduced boundary fault activity but increased activity along the Gaoliu Fault, shifting the sedimentary center to its descending side. The completion of this stage marked significant uplift and denudation of the area, transitioning from extensive Paleogene rifting to the Neogene depression stage (Wu et al. 2022; Pang et al. 2023; Sun et al. 2023b; Zou et al. 2023; Fig. 2).

Stratigraphy

Drilling in the Gaoshangpu oilfield has delineated the stratigraphic sequence from top to bottom, revealing several formations. These include the Pingyuan Formation of the Quaternary (Q), followed by the Neogene's Minghuazhen (Nm) and Guantao (Ng) Formations, and the Dongying (Ed) and Shahejie (Es) Formations of the Paleogene. Notably, the Shahejie Formation is stratified into three subunits, designated Es1, Es2, and Es3 from top to bottom (Jia et al. 2018; Sun et al. 2021; Pang et al. 2023; Zou et al. 2023; Fig. 2).

Data and methods

This study utilized seismic, well-logging, core, and analytical data from the Nanpu Sag. It involved the examination of 740 linear m of cores and 5,000 photographs from 17 wells to analyze typical sedimentary structures. Data from 54 wells and 6 seismic interpretation profiles facilitated the analysis of the sequence cycles, sediment

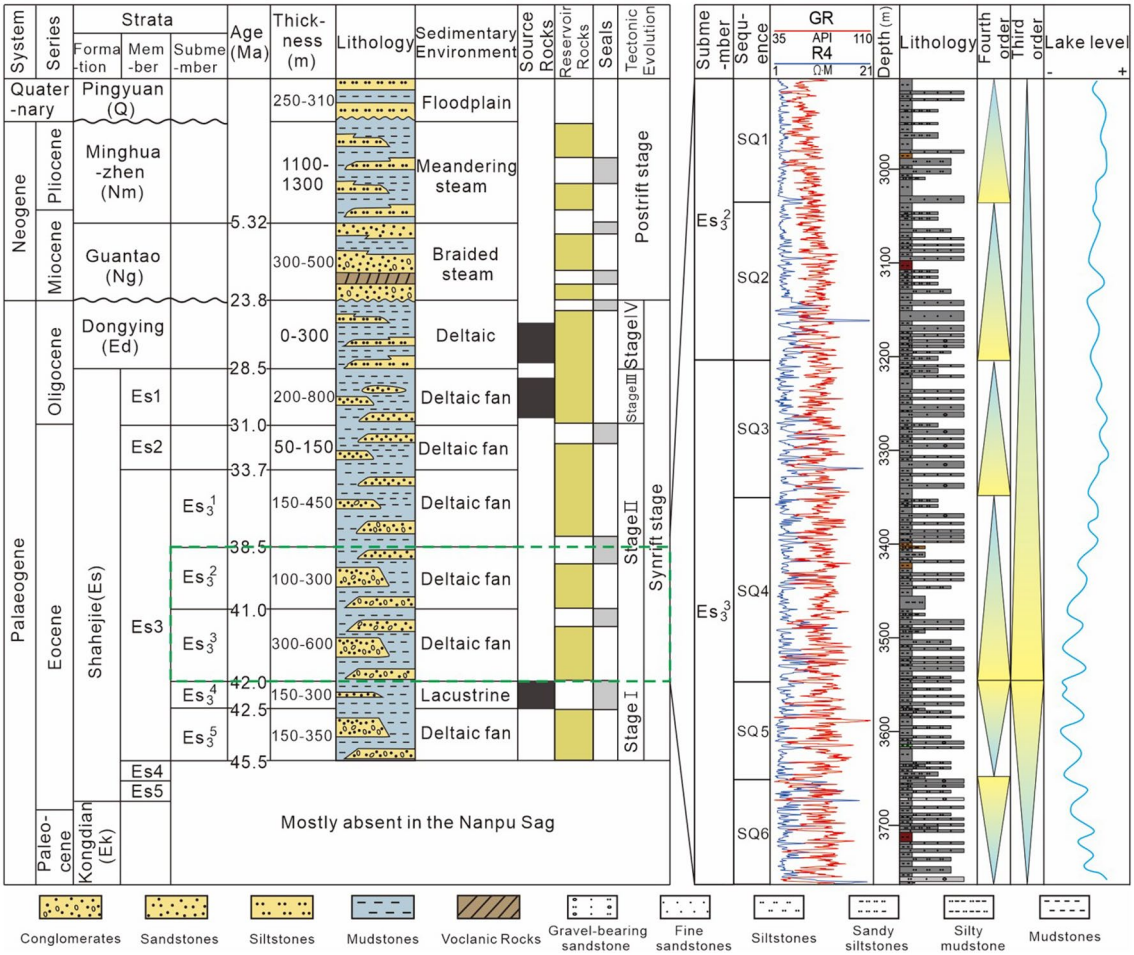

Fig. 2 Sequence stratigraphic chart of Nanpu Sag, Bohai Bay Basin (the left); details lithology and well-logging characteristics at target interval in well G30-30 (the right)

provenance, and sedimentary environments. Petrological analyses were conducted on 116 samples from the Shahejie Formation, focusing on rock type, particle size, weathering, sorting, roundness, and cementation type. Additionally, 23 samples were examined via microscopic sectioning and scanning electron microscopy (SEM) to determine their petrographic characteristics.

Accurate sequence division is critical for understanding sedimentary environments and modeling sedimentary evolution (Yao et al. 2020; Prather et al. 2022). By examining the characteristics of drilling, logging, and seismic profiles, key sequence interfaces can be effectively identified (Makled et al. 2017; Knapp et al. 2019). A comparison of the data from more than 80 wells helped to establish an isochronous stratigraphic sequence framework for the study area (Fig. 3).

In this study, lithological characteristics, typical sedimentary structures, lithofacies successions, single-well sedimentary sequences, and seismic reflection package reflection were observed, identified, and utilized as markers to characterize sedimentary environments and patterns. The structural maturity of clastic rocks, which is indicative of the extent to which clastic sediments have evolved toward their ultimate structural characteristics, is reflected in their particle size, weathering, sorting, roundness, and cementation type. The classification of lithofacies, primarily based on sedimentary structure and lithology, is essential for defining sedimentary environments (Nguidi et al. 2021; Kra et al. 2022; Kane et al. 2023). Analysis of single-well sedimentary sequences includes examining sediment grain size and color variations, lithofacies associations, paleontological characteristics, and sediment–surface contact relationships, which are derived from outcrop and core profiles of the examined stratum. This analysis aids in comparing sedimentary environments. Additionally, seismic reflection package reflection analysis enhances the identification of sedimentary environments by summarizing

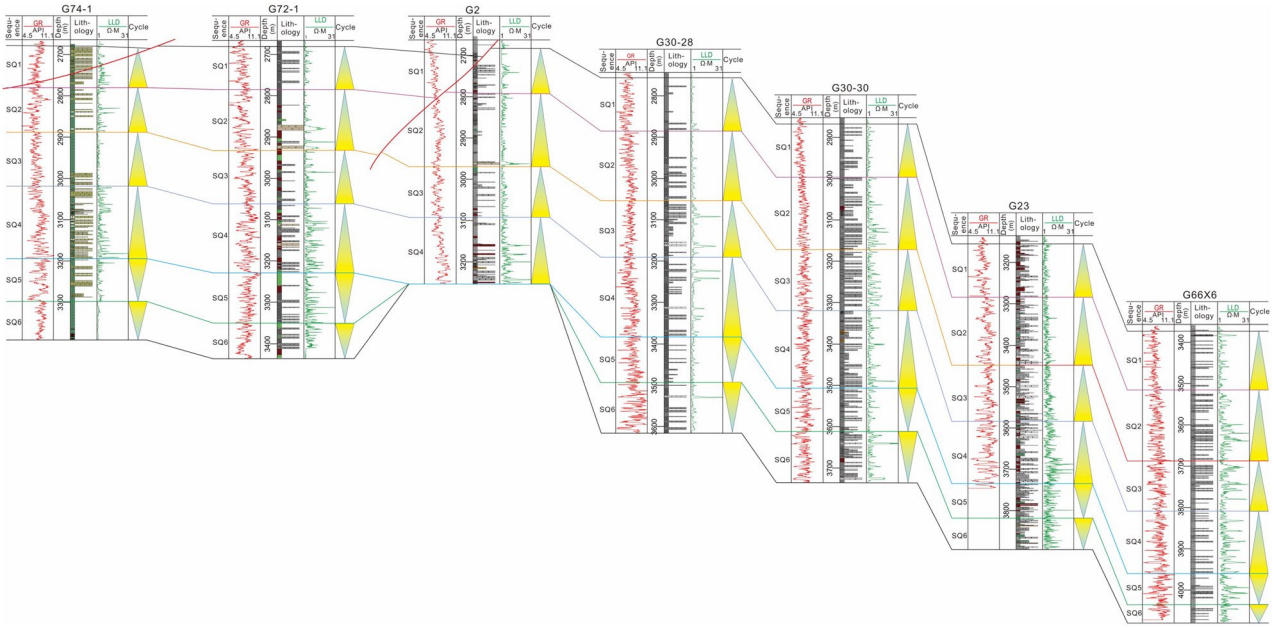

Fig. 3 Sequence stratigraphic framework in Nanpu Sag, Bohai Bay Basin (profile A in Fig. 1)

the responses of seismic profile reflection parameters, such as structure, amplitude, continuity, frequency, and layer velocity (Cukur et al. 2017; Talarico et al. 2020). Unsupervised neural networks facilitate multi-attribute operations, with seismic reflection package reflection classifications based on the amplitude and waveform of input attributes (Wrona et al. 2018). Furthermore, 3D models have been employed to delineate the planar and longitudinal distributions of sedimentary environments. This study integrates sequence division and correlation, structural interpretation, sand body distribution analysis, and sedimentary facies analysis using seismic, well logging, testing, and drilling data. This comprehensive approach has led to the development of stratigraphic and tectonic models, ultimately culminating in sedimentary facies patterns that elucidate the distribution laws of sedimentary facies.

These methodologies have been instrumental in delineating the sedimentary evolution pattern governed by the sequence stratigraphy of the Shahejie Formation in the Nanpu Sag, Bohai Bay Basin, China.

Results

Stratigraphic sequence division

This study, leveraging logging, drilling, and seismic data, performed detailed sequence analysis, division, and comparison of the Shahejie Formation within the Nanpu Sag. The Es_3^{2+3} Formation in the region is categorized into two third-order sequences and six fourth-order sequences. From the base upward, the third-order sequences consist of the regressive system tract (RST) and the transgressive systems tract (TST), which facilitate the establishment of an isochronous stratigraphic correlation framework (Fig. 3).

Third-order stratigraphic sequence division

On the seismic profile, the top of the Es_3^2 sub-member is a set of mudstones, the reflection event is strong and the continuity is good; on the basin boundary, it is the down-lapped surface, which is the top interface of the Es^{2+3} sub-member. The top of the Es_3^4 sub-member is mudstone-oil shale, which shows strong biaxial reflection characteristics, and thick oil shale deposits display the most flooding surface. On the logging curve, acoustic (AC), natural gamma ray (GR), and resistivity (R) data all show high-value characteristics, which is the bottom interface of the Es_3^{2+3} sub-member.

In the seismic profile of the Nanpu Sag, the top interface of the Es_3^2 sub-member consists of a strongly reflective and continuous mudstone layer, representing the down-lapped surface at the basin boundary. This interface also marks the upper limit of the Es_3^{2+3} sub-member. The top of the Es_3^4 sub-member, which comprises mudstone and oil shale, is characterized by strong biaxial reflection and pronounced oil shale deposits that represent the flooding surface. Seismic and logging data, including acoustic (AC), natural gamma ray (GR), and resistivity (R) profiles, highlight high-value attributes at this stratigraphic juncture, delineating the base of the Es_3^{2+3} sub-member.

Analysis of these seismic and drilling interfaces facilitated the division of the Es_3^{2+3} stratum into two third-order sequences: the regressive system tract (RST) and the transgressive system tract (TST). The RST, identifiable by a decrease in lake levels accompanied by fluctuations and an increasing sand–mud ratio, exhibits progradation and a reverse cycle. Conversely, the TST is marked by rising lake levels, accompanied by fluctuations and a decreasing sand–mud ratio, indicative of retrogradation and a positive cycle overall.

Fourth-order stratigraphic sequence division

This study delineated the fourth-order sequences within the third-order sequence boundaries of the Shahejie Formation in the Nanpu Sag. The transgressive system tract (TST) includes two sequences, SQ6 (Sequence 6) and SQ5 (Sequence 5), located in the lower part of the Es_3^3 sub-member, while four sequences, SQ4 (Sequence 4), SQ3 (Sequence 3), SQ2 (Sequence 2), and SQ1 (Sequence 1), were identified within the regressive system tract (RST) in the upper part of the Es_3^3 sub-member and the Es_3^2 sub-member (Figs. 2, 3). Each fourth-order sequence boundary, which is aligned on the same phase axis on the seismic section, demonstrates good continuity and is easily traceable across the study area.

In SQ6, the relative lake level consistently declined, exhibiting frequent fluctuations. This led to the deposition of light-gray fine-grained sandstone and brown-gray mudstone in alternating layers, which is a characteristic of a reverse cycle (Fig. 2). The substantial mudstone layer at the base represents the maximum flooding surface, serving as a comparative marker layer. The strata, varying in thickness from 90 to 220 m and reaching depths between 3800 and 4200 m, correspond to several wells drilled in this study area.

The top interface of SQ5 serves as a sedimentary conversion surface characterized by a reverse depositional cycle, where coarse-grained sediments overlay fine-grained sediments. This interface exhibits medium–low amplitude electrical properties such as box, bell, and tooth types (GR, RD). Throughout SQ5, the relative lake level gradually declined, showing fluctuations and reaching its lowest point at the end of the sequence. The lithologic composition is primarily gray and brownish-yellow pebbly sandstone, mixed with coarse- and medium-grained sandstone and brownish-gray mudstone. This sequence demonstrates upward progradation, with a thickness ranging from 105 to 235 m and a burial depth between 3300 and 4100 m (Fig. 2).

In SQ4, the relative lake level continued to rise, exhibiting frequent fluctuations. The basal section of SQ4, characterized by a lithologic mutation surface, transitions from coarse-grained sediments at the bottom to fine-grained sediments at the top. This section comprises brownish-yellow and gray pebbly sandstone, coarse- and fine-grained sand, and argillaceous sandstone intermixed with grayish-green and brownish-gray mudstone (Fig. 2). The strata vary in thickness from 120 to 200 m and have burial depths ranging from 3200 to 4000 m. The electrical properties such as the gamma-ray (GR) and resistivity (RD) properties, display box, bell, and tooth patterns with medium–low amplitudes; notably, the resistivity curve shows high values at the base and decreases progressively upward (Fig. 2). This interval is a principal oil-producing zone, which is extensively distributed across the study area.

The relative lake level of SQ3 increased gradually, exhibiting minor fluctuations. This sequence consists of brown-yellow glutenite, medium to coarse-grained sandstone, and gray to brown-gray mudstone interbedding, indicating a normal depositional cycle. The strata thickness values range from 110 to 155 m, with burial depths ranging from approximately 3050 to 3970 m (Fig. 2).

In SQ2, the lake level also rose gradually but with fewer fluctuations. Here, the lithology transitions from coarse at the bottom to fine-grained at the top, reflecting a normal cycle of deposition dominated by mudstone. The thickness values of individual sandstone layers diminish, alongside a decrease in the frequency of sand–mud interbedding. The strata range from 150 to 225 m in thickness and are buried at depths ranging from 2950 to 3850 m (Fig. 2). Vertically, this sequence predominantly exhibits retrogradational patterns, with gamma-ray (GR) logging revealing low-amplitude funnel and tooth patterns.

SQ1 experienced a gradual increase in lake level without significant fluctuations, culminating in the maximum flooding surface (MFS) when the water level was at its highest. Composed predominantly of fine sediments and dark-gray and brown-gray mudstone with layers of very fine to fine-grained sandstone, this sequence was deposited during a normal cycle. The strata thickness varies from 80 to 140 m, with burial depths between 2770 and 3600 m. It acts as a widely distributed marker bed and regional cap rock for the lower oil layer in this area (Fig. 2).

The lithological analysis of the regressive system tract (RST) in the lower part of the study area reveals coarser sediments progressing upward, as indicated by progradational patterns on the logging curves and weak reflectivity with poor continuity on the seismic profiles. Conversely, the transgressive system tract (TST) developed during a period of significant expansion of water bodies and exhibits finer sediments upward with most wells primarily containing large sets of mudstones in SQ1. This stratification is marked by retrogradational trends on the logging curves (Fig. 3). In the seismic

profile, the TST is characterized by increasing reflection intensity from weak to strong, demonstrating improved continuity across the sequence.

Sediment provenance

Paleo-geomorphological analysis of the Es_3^{2+3} sub-member within the Gaobei slope belt revealed that the sedimentary center is located north of the Gaoshangpu structural belt and west of the Liuzan structural belt. The basin has significant faulting, resulting in its subdivision into multiple secondary sags (Fig. 4). The northern part of the study area includes the Xinanzhuang and Baigezhuang Uplifts, which provided the sediments essential for the development of the area's sedimentary system (Fig. 4).

Lithological characteristics

Rock type and compositional maturity

Analysis and statistical review of core samples from the Es_3^{2+3} sub-member in the study area reveal that the sandstones predominantly consist of lithic arkose and feldspathic litharenite (Fig. 5). In SQ1, the samples are primarily composed of lithic arkose and feldspathic litharenite, with minor amounts of litharenite and arkose. These samples have low quartz contents and low compositional maturity (Fig. 5a). The lithology of SQ2 mirrors that of SQ1 but with an increased presence of stable components such as quartz, although its compositional maturity remains low (Fig. 5b). In SQ3, feldspathic litharenite is the most abundant, followed by lithic arkose, with less litharenite and arkose. Here, the quartz content and component maturity are greater than those in SQ2 (Fig. 5c). SQ4 is similarly dominated by lithic arkose and feldspathic litharenite, but with fewer occurrences of arkose and litharenite, it features a broader range of quartz content values than SQ3 (Fig. 5d). SQ5 is primarily composed of lithic arkose and feldspathic litharenite and is occasionally interspersed with litharenite (Fig. 5e). Fewer samples are available from SQ6 (Fig. 5f).

Scanning electron microscopy (SEM) and electron microscope images reveal that the primary minerals in the Es_3^{2+3} sub-member in the study area are predominantly quartz, feldspar, and clay minerals (Fig. 6A–L). Quartz exhibits varying degrees of overgrowth (Fig. 6A, J, L), while feldspar shows different levels of albitization, particularly in plagioclase (Fig. 6C, J). Additionally, several clay minerals are evident, including illite (Fig. 6A, G), illite/smectite (Fig. 6B, E–G), pyrite (Fig. 6B), albite (Fig. 6C, I), chlorite (Fig. 6D–H), and mica (Fig. 6M). The transformation of kaolinite to illite and chlorite is notable (Fig. 6F). Early compaction led to the formation of carbonate cement, which effectively sealed the intergranular pore system (Fig. 6J), and these pores were often filled with crude oil (Fig. 6K). Pore compaction is particularly pronounced in clay-rich, soft-grained, and fine-grained sandstone (Fig. 6K). Various types of pores have developed, including dissolved and intergranular pores; with notable distinctions in expanded and reduced intergranular pores, the latter exhibit further erosion post-compaction (Fig. 6L). The study area also features oolitic limestone and biological shells, predominantly in regions either uplifted underwater or devoid of terrigenous sediments (Fig. 6N, O).

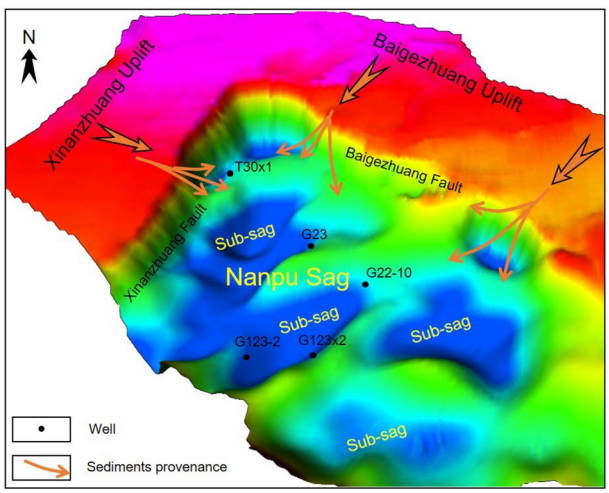

Fig. 4 Palaeogeomorphic characteristics of the Nanpu Sag, Bohai Bay Basin

Maturity of clastic rocks

In the Es_3^{2+3} sub-member of the study area, the mineral composition of clastic rock particles consists of 28% quartz, 35.5% feldspar, and 36.5% rock debris, resulting in an average maturity index of 0.39. This low maturity index indicates a proximal source for the sediments, which underwent minimal transport before deposition in the basin. The higher proportions of feldspar and rock debris further substantiate the short transport distance and rapid accumulation of sediment (Li et al. 2021).

Analysis of structural maturity in the Es_3^{2+3} sub-member of the Nanpu Sag reveals a low maturity level, characterized by weathering ranging from low to deep, and roundness varying from sub-angular to sub-rounded, coupled with poor to good sorting. These characteristics suggest that sediment transport was short-range (Table 1). In SQ1, the particle sizes primarily range from 0.1 to 0.4 mm, exhibiting moderate to deep weathering, moderate sorting, and primarily sub-angular to sub-rounded roundness. The predominant cementation type is porous, although a variety of cementation types are present (Table 1). The SQ2 particles range from 0.1

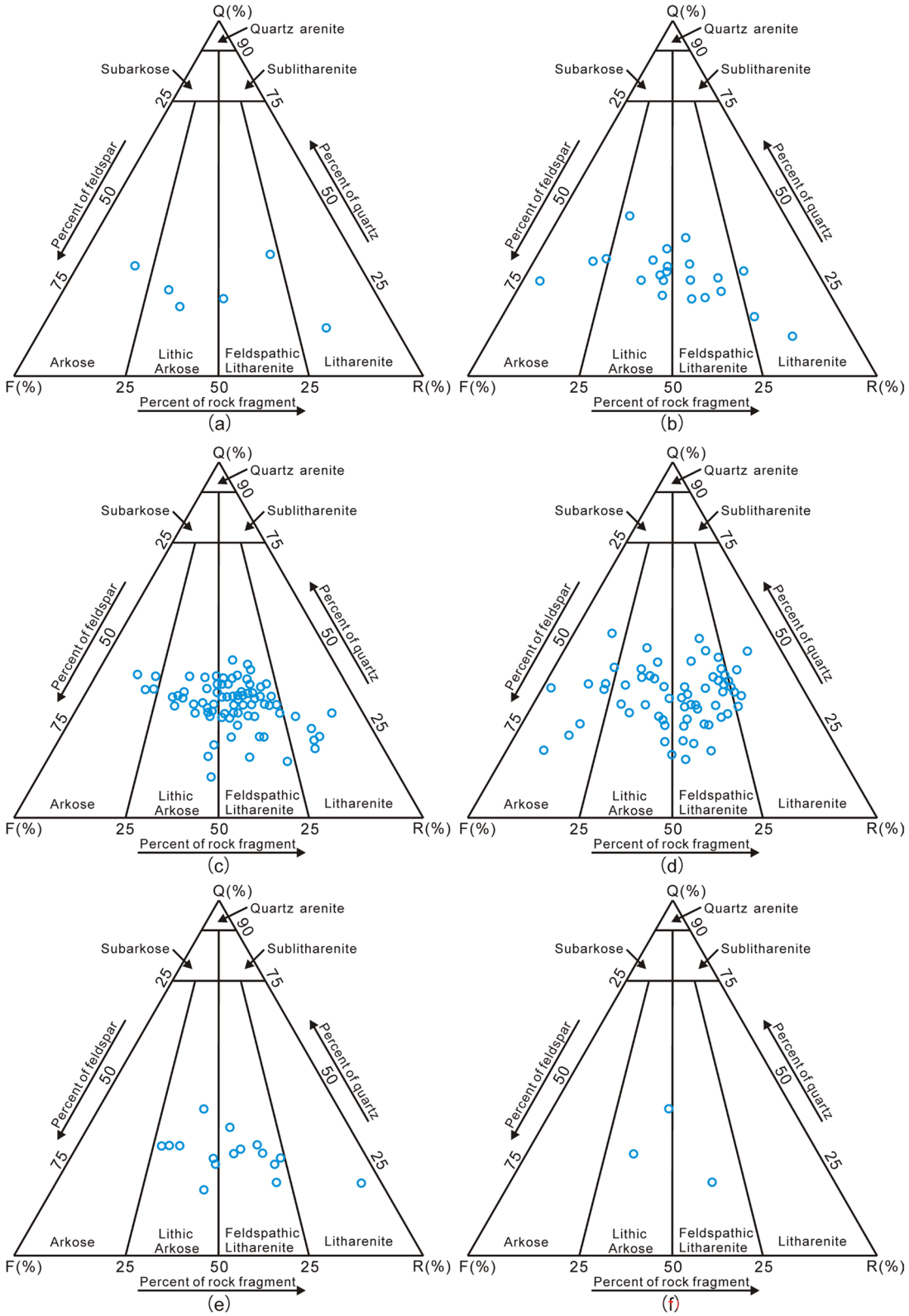

Fig. 5 Sandstone type of the Shahejie Formation in Nanpu Sag, Bohai Bay Basin. **a** SQ1; **b** SQ2; **c** SQ3; **d** SQ4; **e** SQ5; **f** SQ6

to 0.9 mm in length with mostly moderate weathering and sorting and similar roundness and diverse cementation types, including porous cementation, basal cementation, basal–porous cementation, contact cementation, porous–contact cementation, contact–film cementation, contact–crystal cementation, and other cementation varieties (Table 1). SQ3 has particle sizes ranging from 0.1 to 0.45 mm, with conditions similar to those of SQ2, including comparable cementation types (Table 1). SQ4 particles range from 0.05 to 0.5 mm in size, feature a broad spectrum of weathering from low to deep, and exhibit variable sorting from poor to good. The roundness typically ranges from sub-angular to sub-rounded, with diverse cementation types noted (Table 1). In SQ5, the particle sizes are mostly 0.07–0.4 mm with low-to-moderate weathering and moderate-to-good sorting. The roundness and cementation types are similar to those of earlier sequences (Table 1). Finally, SQ6 features particle sizes ranging from 0.1 to 0.5 mm, moderate weathering, sorting, and sub-angular to sub-rounded roundness, with diverse cementation observed (Table 1).

Sedimentary lithofacies

Analysis of sedimentary structures in the Nanpu Sag core reveals a variety of formations. These include normal graded-bedding (Fig. 7A1, B2–B4, D1), through cross-bedding (Fig. 7A2–A7, B5–B7, C6, C7), inverse graded-bedding (Fig. 7B1), low-angle cross-bedding (Fig. 7C1, C4), high-angle cross-bedding (Fig. 7C2, C3, C5), massive-bedding (Fig. 7D2–D5), and fault planes (Fig. 7D3, E7). Additionally, parallel-bedding (Fig. 7D6, D7, E1, E2), ripple cross-bedding (Fig. 7E3–E5), wavy-bedding, and lenticular-bedding (Fig. 7E6) are evident. The core also includes mud layers (Fig. 7F1–F4) and erosion surfaces (Fig. 7, F5–F7).

The sedimentary characteristics of the Es_3^{2+3} submember in the Nanpu Sag were have been extensively studied, and 22 lithofacies types within conglomerates, sandstones, and mudstones have been identified (Fig. 8). These lithofacies include fine-grained conglomerate with massive-bedding (FcM) and through cross-bedding (FcT); glutenite with inverse graded-bedding (GI) and normal graded-bedding (GN); gravel-bearing coarse-grained sandstone with massive-bedding (GcM) and through cross-bedding (GcT); coarse-grained sandstone with through cross-bedding (CT); medium-grained sandstone with high-angle cross-bedding (MeH), through cross-bedding (MeT), and massive-bedding (MeM); gravel-bearing medium-grained sandstone with parallel-bedding (GmP); fine-grained sandstones with massive-bedding (FiM), through cross-bedding (FiT), parallel-bedding (FiP), and low-angle cross-bedding (FiL); sandstones with inverse graded-bedding (SI) and normal graded-bedding (SN); argillaceous siltstone with ripple cross-bedding (AsR); siltstone with wave-bedding and lenticular-bedding (SiW), and ripple cross-bedding (SiR); and mud with horizontal-bedding (MH) and massive-bedding (MM).

Single-well sedimentary sequence

Analysis of the single-well sedimentary sequence for well G66-5, which penetrated SQ3 and SQ4, indicates a dominant fan delta sedimentary environment (Fig. 9). SQ4 features layers progressing from gray-celadon mudstone at the base to very fine to fine-grained sandstone, pebbly sandy conglomerate, and light-gray coarse-grained sandstone with trough cross-bedding at the top, with visible oil and gas traces in the sandstone strata. The lithological sequence correlates well with the logging data, the GR logging curve displays a low-value box type, while the RLLD logging curve exhibits high values. In the lower section of SQ3 (4358–4366 m), the sequence comprises light-gray mudstone with intervals of bluish very fine to fine-grained sandstone, conglomerate, glutenite, and coarse sandstone, all displaying trough cross-bedding (Fig. 9). Notably, there is a distinct erosional surface at the base of the sandy conglomerate strata. The GR and RLLD logging curves both show box-type configurations, with oil traces, patches, and imprints evident in the reservoir. The upper section of SQ3 (4285–4293.5 m) includes

(See figure on next page.)

Fig. 6 Microscopic sections and SEM images exhibiting petrographic characteristics of the Shahejie Formation in Nanpu Sag, Bohai Bay Basin. **A** Q: quartz, quartz overgrowth, Il: illite, G65-1, 3222.50 m; **B** Q: quartz, Py: pyrite, illite/smectite, G66X3, 4074.62 m; **C** Fel: feldspar, albitization characteristics of plagioclase, Al: albite, G66X3, 4074.62 m; **D** Q: quartz, Ch: chlorite, G32-30,3476.55 m; **E** Ch: chlorite, illite/smectite, G66X3, 4074.62 m; **F** Ch: chlorite, illite/smectite, Kao: kaolinite, kaolinite converted to illite and chlorite, G65-1, 3222.52 m; **G** Fel: feldspar, feldspar quartz overgrowth, albitization characteristics of plagioclase, Il: illite, illite/smectite, G65-1, 3222.52 m; **H** Ch: chlorite, G139X9, 3640.33 m; **I** Fel: feldspar, feldspar quartz overgrowth, albitization characteristics of plagioclase, Al: albite, G66X3, 4074.62 m; **J** Q: quartz, Fel: feldspar, Cal: calcite, carbonate cements following early compaction seal the intergranular pore system, G30-32-3, 4074.62 m; **K** Cr: crude oil, Rf: rock fracture, the pore compaction of rich clay, soft grain sandstone and fine grain sandstone is strong, G32-30, 4074.62 m; **L** Q: quartz, Di: dissolved pore, intergranular pores, mainly intergranular dissolved pores, include expanded intergranular pores and reduced intergranular pores, the reduced intergranular pores is further eroded after pore compression, G23-3, 4074.62 m; **M** Mi: mica, G5-1, 4074.62 m; **N** Oo: oolitic limestone, Bs: biological shell, developed on an underwater uplift or devoid of terrigenous sediments, G8, 4074.62 m; **O** Oo: oolitic limestone, Bs: biological shell, G8-2, 4074.62 m

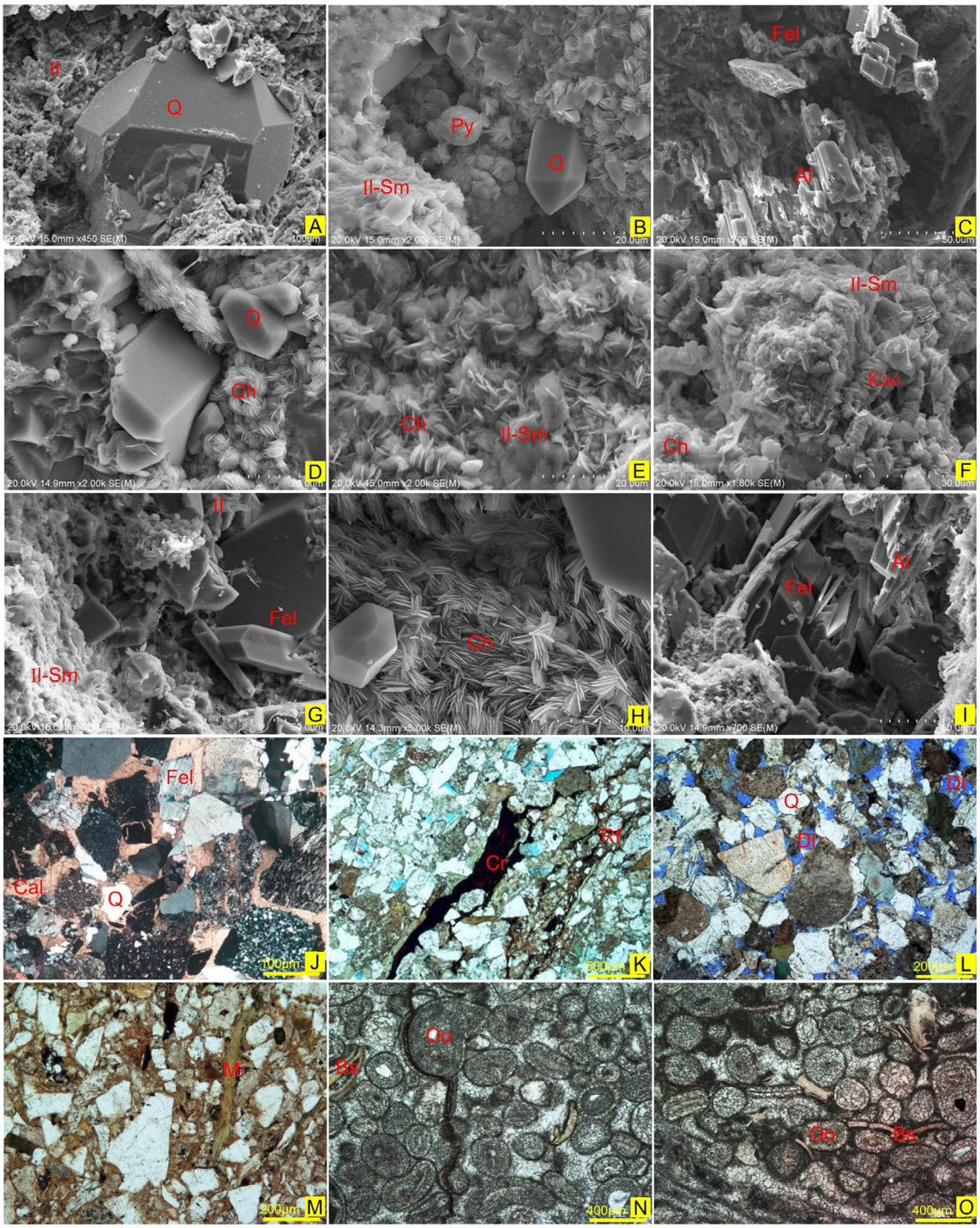

Fig. 6 (See legend on previous page.)

a sequence from conglomerate with reverse graded-bedding at the base to coarse-grained sandstone with through cross-bedding, medium-grained sandstone with parallel cross-bedding, and fine-grained sandstone with ripple cross-bedding, culminating in very fine-grained sandstone with ripple cross-bedding and dark-gray mudstone. The sequence concludes with conglomerate exhibiting reverse and normal graded-bedding, and fine-grained sandstone with cross-bedding at the top. Both the GR and RLLD logging curves maintain box-type

Table 1 Petrological parameters statistical table of the Shahejie Formation in Nanpu Sag, Bohai Bay Basin

No.	Well	Sequence	Depth (m)	Particle size (mm)	Weathering	Sorting	Roundness	Cementation type
1	G1	SQ1	3020	0.14–0.19	Moderate–deep	Good	Sub-rounded	Basal cementation
2	G2	SQ1	2775	0.15–0.35	Moderate	Moderate	Sub-angular	Porous cementation
3	G2	SQ1	2792	0.1–0.4	Deep	Moderate	Sub-rounded	Porous cementation
4	G22	SQ1	4072	0.1–0.35	Moderate	Moderate	Sub-angular–sub-rounded	Contact cementation
5	G23	SQ1	3163	0.8–2.5	Low	Moderate	Sub-angular–sub-rounded	Basal–porous cementation
6	G23	SQ1	3236.4	0.01–0.05	Moderate	Good	Sub-angular	Basal–porous cementation
7	G4	SQ1	2570.68	0.05–0.20	Deep	Moderate	Sub-angular–sub-rounded	Porous cementation
8	G4	SQ1	2573.55	0.05–0.20	Deep	Moderate	Sub-angular–sub-rounded	Porous cementation
9	G4	SQ1	2580.36	0.1–0.25	Deep	Moderate	Sub-angular–sub-rounded	Porous cementation
10	G1	SQ2	3160	0.05–0.20	Moderate	Moderate	Sub-angular–sub-rounded	Porous cementation
11	G1	SQ2	3176.4	0.02–0.1	Deep	Moderate	Sub-angular	Porous cementation
12	G1	SQ2	3179	0.25–0.9	Moderate	Moderate	Sub-rounded	Basal–porous cementation
13	G14	SQ2	3430.81	0.1–0.25	Moderate–deep	Good	Sub-angular–sub-rounded	Contact cementation
14	G14	SQ2	3500	0.15–0.25	Low–moderate	Good	Sub-rounded	Contact cementation
15	G2	SQ2	2825	0.01–0.03	Moderate	Moderate	Sub-rounded	Basal cementation
16	G22	SQ2	4074	0.25–0.5	Moderate	Good	Sub-angular–sub-rounded	Contact cementation
17	G22	SQ2	4108	0.15–0.1	Moderate–deep	Good	Sub-angular–sub-rounded	Contact cementation
18	G22	SQ2	4118	0.3–0.7	Moderate–deep	Moderate	Sub-rounded	Contact cementation
19	G23	SQ2	3416	0.05–0.15	Low	Moderate	Sub-angular–sub-rounded	Porous–contact cementation
20	G3104	SQ2	3200.2	0.12–0.33	Low–moderate	Moderate	Sub-angular–sub-rounded	Contact–film cementation
21	G3104	SQ2	3203.47	0.5–1.1	Moderate	Poorly	Sub-rounded	Contact cementation
22	G3104	SQ2	3204.04	0.01–0.05	Low	Good	Sub-angular	Porous–contact cementation
23	G3104	SQ2	3240.78	0.25–0.7	Low	Moderate	Sub-rounded	Contact–crystal cementation
24	G4	SQ2	2675.81	0.1–0.25	Moderate	Moderate	Sub-angular–sub-rounded	Porous cementation
25	G65	SQ2	2980.15	0.1–0.25	Moderate	Moderate	Sub-angular	Basal–porous cementation
26	G65	SQ2	2985.89	0.03–0.25	Moderate	Poorly	Sub-angular	Basal–porous cementation
27	G65	SQ2	2986.28	0.1–0.25	Low	Good	Sub-rounded	Contact–porous cementation
28	G65	SQ2	2990.71	0.1–0.25	Deep	Moderate	Sub-angular–sub-rounded	Film-porous cementation
29	G65	SQ2	3002.36	0.1–0.25	Deep	Poorly	Sub-angular–sub-rounded	Basal cementation
30	G65	SQ2	3007.28	0.03–0.25	Moderate	Poorly	Sub-angular–sub-rounded	Film–porous cementation
31	G82	SQ2	3611.08	0.15–0.50	Moderate	Moderate	Sub-angular–sub-rounded	Porous cementation
32	G82	SQ2	3618.86	0.10–0.25	Moderate	Moderate	Sub-angular–sub-rounded	Contact cementation

Table 1 (continued)

No.	Well	Sequence	Depth (m)	Particle size (mm)	Weathering	Sorting	Roundness	Cementation type
33	G82	SQ2	3628.59	0.10–0.25	Moderate	Moderate	Sub-angular–sub-rounded	Contact cementation
34	G1	SQ3	3210	0.10–0.25	Moderate–deep	Moderate	Sub-rounded	Contact–porous cementation
35	G1	SQ3	3269	0.05–0.10	Moderate–deep	Moderate–poorly	Sub-rounded	Contact cementation
36	G11	SQ3	3510	0.25–0.45	Moderate	Good	Sub-angular–sub-rounded	Contact–porous cementation
37	G11	SQ3	3530	0.1–0.4	Moderate	Good	Sub-angular–sub-rounded	Contact–porous cementation
38	G14	SQ3	3542	0.25–0.4	Low	Good	Sub-rounded	Contact–crystal cementation
39	G14	SQ3	3615	0.15–0.3	Low	Moderate	Sub-rounded	Contact–crystal cementation
40	G14	SQ3	3630	0.5–0.8	Low–moderate	Good	Sub-rounded	Contact–crystal cementation
41	G14	SQ3	3650	0.05–0.2	Low–moderate	Moderate	Sub-angular–sub-rounded	Contact–film cementation
42	G14	SQ3	3662	0.25–0.5	Moderate–deep	Good	Sub-rounded	Contact–crystal cementation
43	G2	SQ3	3035	0.1–0.25	Moderate–deep	Good	Sub-angular–sub-rounded	Porous cementation
44	G2	SQ3	3050	0.1–0.25	Moderate	Good	Sub-angular–sub-rounded	Contact–fill cementation
45	G23	SQ3	3562.01	0.02–0.1	Low–moderate	Moderate	Sub-angular–sub-rounded	Contact–porous cementation
46	G23	SQ3	3569.67	0.1–0.25	Low	Good	Sub-angular–sub-rounded	Contact–porous cementation
47	G23	SQ3	3575.06	0.01–0.1	Low	Moderate	Sub-angular	Basal cementation
48	G5	SQ3	3125	0.25–0.6	Moderate	Moderate	Sub-rounded	Contact cementation
49	G5	SQ3	3150	0.1–0.25	Moderate	Good	Sub-angular–sub-rounded	Porous cementation
50	G5	SQ3	3175.37	0.02–0.2	Moderate	Moderate	Sub-angular	Basal–porous cementation
51	G5	SQ3	3181.32	0.02–0.2	Moderate	Moderate	Sub-angular	Basal–porous cementation
52	G5	SQ3	3190.79	0.15–0.35	Deep	Moderate	Sub-angular–sub-rounded	Porous cementation
53	G5	SQ3	3205.31	0.15–0.25	Deep	Good	Sub-angular–sub-rounded	Contact cementation
54	G5	SQ3	3216.23	0.1–0.4	Moderate–deep	Moderate	Sub-angular–sub-rounded	Porous cementation
55	G2	SQ4	3105	0.5–0.8	Moderate	Poorly	Sub-angular–sub-rounded	Contact cementation
56	G2	SQ4	3130	0.1–0.25	Moderate–deep	Moderate	Sub-angular–sub-rounded	Porous–fill cementation
57	G2	SQ4	3135	0.1–0.25	Moderate–deep	Good	Sub-angular–sub-rounded	Porous cementation
58	G2	SQ4	3155	0.1–0.25	Moderate	Good	Sub-rounded	Contact cementation
59	G2	SQ4	3170	0.1–0.25	Moderate	Good	Sub-angular–sub-rounded	Porous cementation
60	G2	SQ4	3177	0.2–0.5	Moderate–deep	Moderate	Sub-rounded	Contact cementation
61	G23	SQ4	3589.13	0.15–0.5	Low	Moderate	Sub-rounded	Contact–film cementation
62	G23	SQ4	3594.87	0.02–0.05	Low	Moderate	Sub-angular–sub-rounded	Film-porous cementation

Table 1 (continued)

No.	Well	Sequence	Depth (m)	Particle size (mm)	Weathering	Sorting	Roundness	Cementation type
63	G23	SQ4	3601	0.25–0.5	Low	Good	Sub-angular–sub-rounded	Contact cementation
64	G23	SQ4	3720	0.25–0.4	Low	Good	Sub-angular–sub-rounded	Contact cementation
65	G23	SQ4	3760	0.02–0.1	Moderate	Moderate	Sub-angular	Porous cementation
66	G23	SQ4	3780	0.13–0.23	Low	Good	Sub-rounded	Contact–porous cementation
67	G23	SQ4	3796	0.15–0.4	Moderate	Moderate	Sub-angular–sub-rounded	Contact–porous cementation
68	G23	SQ4	3833	0.05–0.15	Moderate	Moderate	Sub-angular–sub-rounded	Contact cementation
69	G23	SQ4	3878	0.05–0.5	Low–moderate	Good	Sub-rounded	Contact cementation
70	G26	SQ4	3783	0.25–0.4	Low	Moderate	Sub-angular–sub-rounded	Contact cementation
71	G26	SQ4	3805	0.25–0.5	Low–moderate	Good	Sub-rounded	Contact cementation
72	G26	SQ4	3855	0.25–0.5	Low–moderate	Good	Sub-rounded	Contact–crystal cementation
73	G26	SQ4	3862.4	0.25–0.5	Low	Good	Sub-angular–sub-rounded	Contact cementation
74	G26	SQ4	3882	0.1–0.25	Low	Good	Sub-rounded	Contact cementation
75	G5	SQ4	3223.75	0.08–0.2	Moderate–deep	Moderate	Sub-angular–sub-rounded	Porous cementation
76	G5	SQ4	3226.3	0.05–0.1	Moderate	Good	Sub-angular–sub-rounded	Contact cementation
77	G5	SQ4	3231	0.01–0.25	Moderate	Poorly	Sub-rounded	Basal cementation
78	G5	SQ4	3236.3	0.4–1.8	Moderate	Poorly	Sub-rounded	Porous cementation
79	G5	SQ4	3242.2	0.4–1	Moderate	Moderate	Sub-rounded	Contact cementation
80	G5	SQ4	3250	0.05–0.15	Moderate	Moderate	Sub-angular–sub-rounded	Contact cementation
81	G5	SQ4	3268	0.05–0.25	Moderate	Moderate	Sub-angular–sub-rounded	Contact–porous cementation
82	G5	SQ4	3292	0.05–0.15	Moderate	Moderate	Sub-angular–sub-rounded	Contact cementation
83	G5	SQ4	3312	0.1–0.25	Moderate	Good	Sub-angular	Contact–porous cementation
84	G5	SQ4	3318	0.1–0.25	Moderate	Good	Sub-rounded	Contact–porous cementation
85	G5	SQ4	3341	0.1–0.25	Moderate	Good	Sub-rounded	Contact–porous cementation
86	G5	SQ4	3352	0.1–0.25	Moderate	Good	Sub-rounded	Contact cementation
87	G5	SQ4	3382	0.1–0.25	Moderate	Good	Sub-angular–sub-rounded	Porous cementation
88	G74-1	SQ4	3131.71	0.1–0.03	Moderate–deep	Poorly	Sub-angular	Basal cementation
89	G74-1	SQ4	3133.25	0.25–0.03	Moderate–deep	Poorly	Sub-angular–sub-rounded	Basal–porous cementation
90	G74-1	SQ4	3135	0.25–0.03	Moderate–deep	Poorly	Sub-angular–sub-rounded	Basal cementation
91	G74-1	SQ4	3141.73	0.01–0.03	Moderate–deep	Moderate	Sub-angular–sub-rounded	Basal cementation
92	G74-1	SQ4	3143	0.25–0.1	Moderate–deep	Moderate	Sub-angular–sub-rounded	Basal–porous cementation
93	G74-1	SQ4	3147.28	0.25–0.1	Moderate-deep	Poorly	Sub-angular–sub-rounded	Film–porous cementation
94	G74-1	SQ4	3149.59	0.1–0.03	Moderate	Poorly	Sub-angular	Contact–porous cementation

Table 1 (continued)

No.	Well	Sequence	Depth (m)	Particle size (mm)	Weathering	Sorting	Roundness	Cementation type
95	G74-1	SQ4	3152.76	0.25–0.03	Moderate	Poorly	Sub-angular–sub-rounded	Basal–porous cementation
96	G74-1	SQ4	3154.48	0.1–0.13	Moderate-deep	Poorly	Sub-angular	Contact–porous cementation
97	G1	SQ5	3410	0.02–0.3	Deep	Moderate	Sub-angular	Porous cementation
98	G1	SQ5	3450	0.1–0.35	Deep	Moderate	Sub-angular	Basal cementation
99	G26	SQ5	3932	0.25–0.5	Low	Good	Sub-rounded	Contact–fill cementation
100	G26	SQ5	3934	0.15–0.25	Low	Good	Sub-angular–sub-rounded	Contact cementation
101	G26	SQ5	3952	0.3–0.5	Low	Good	Sub-rounded	Contact cementation
102	G26	SQ5	3970	0.15–0.25	Low	Good	Sub-rounded	Contact–porous cementation
103	G5	SQ5	3425	0.1–0.25	Moderate	Good	Sub-rounded	Crystal cementation
104	G5	SQ5	3445	0.08–0.23	Moderate	Moderate	Sub-angular–sub-rounded	Crystal cementation
105	G5	SQ5	3448	0.12–0.4	Moderate	Moderate	Sub-rounded	Contact cementation
106	G5	SQ5	3459	0.15–0.25	Low	Good	Sub-rounded	Porous cementation
107	G5	SQ5	3481	0.1–0.25	Moderate	Good	Sub-rounded	Contact cementation
108	G5	SQ5	3488	0.07–0.25	Moderate	Moderate	Sub-rounded	Contact–porous cementation
109	G5	SQ5	3502	0.09–0.24	Moderate	Moderate	Sub-rounded	Dissolution–porous cementation
110	G5	SQ5	3521	0.2–0.4	Moderate	Moderate	Sub-angular–sub-rounded	Contact cementation
111	G1	SQ6	3457.2	0.25–0.5	Moderate	Moderate	Sub-rounded	Contact–porous cementation
112	G1	SQ6	3490	0.1–0.25	Deep	Good	Sub-angular–sub-rounded	Porous cementation
113	G1	SQ6	3550	0.15–0.5	Deep	Moderate	Sub-angular–sub-rounded	Contact–porous cementation
114	G26	SQ6	3974.4	0.25–0.5	Low	Good	Sub-angular–sub-rounded	Contact cementation
115	G26	SQ6	3977	0.12–0.25	Low–moderate	Good	Sub-angular–sub-rounded	Contact–fill cementation
116	G26	SQ6	3987	0.15–0.3	Low–moderate	Moderate	Sub-rounded	Contact cementation

configurations, with further indications of oil traces and patches within the reservoir (Fig. 9).

Seismic reflection characteristics

Three fundamental seismic reflection package reflection types have been identified in the study area (Fig. 10). The top interface of SQ1 is characterized by a medium to strong amplitude reflection that is continuous and easily traceable, indicative of a regional unconformity. This layer predominantly features continuous, parallel to sub-parallel seismic reflection package reflection with medium to strong amplitude, interspersed with areas of medium amplitude and chaotic reflections. The predominant lithology consists of stable mudstone and fine-grained sediments (Fig. 10a). The seismic signature of SQ2 features both medium to strong and weak amplitude, continuous parallel to sub-parallel seismic reflection package reflection. The upper lithology comprises fine-grained sandstone, transitioning to coarser sandy conglomerate downward (Fig. 10b). The seismic response of SQ3 displays medium to strong amplitude and medium continuity in parallel to sub-parallel seismic reflection package reflection, with sheet seismic reflection package reflection occurring in parts of the region. The formation mainly consists of sandy conglomerate and medium- to coarse-grained sandstone with mudstone interbedding, transitioning from coarse-grained at the bottom to fine-grained at the top (Fig. 10c). SQ4 is characterized by medium amplitude, continuous parallel to sub-parallel seismic reflection package reflection, incorporating lenticular seismic reflection package reflection locally. The lithology transitions from coarse-grained at the bottom to fine-grained at the top, consisting of brownish-yellow and gray pebbly sandstone,

Fig. 7 Typical sedimentary structures of the Shahejie Formation in Nanpu Sag, Bohai Bay Basin. A1: Normal graded cross-bedding, G66×5, A2: Through cross-bedding, G66×5, A3: Through cross-bedding, G3×3, A4: Through cross-bedding, G5, A5: Through cross-bedding, G123×9, A6: Through cross-bedding, oil trace, G3×3, A7: Through cross-bedding, G66, B1: Inverse graded cross-bedding, G66×5, B2: Normal graded cross-bedding, very coarse-grained, G66-3, B3: Normal graded cross-bedding, G66-1, B4: Normal graded cross-bedding, G66-3, B5: Through cross-bedding, G19-10, B6: Through cross-bedding, oil trace, G19-10, B7: Through cross-bedding, G82, C1: Low angle cross-bedding, G82, C2: High angle cross-bedding, G83-10, C3: High angle cross-bedding, G3×3, C4: Low angle cross-bedding, G19-10, C5: High angle cross-bedding, G66×5, C6: Through cross-bedding, G5, C7: Through cross-bedding, G3104, D1: Normal graded cross-bedding, G66, D2: Massive bedding, G66×5, D3: Massive bedding, fault plane, G5, D4: Massive bedding, oil trace, G5, D5: Massive bedding, G5, D6: Parallel bedding, G123×9, D7: Parallel bedding, G123×9, E1: Parallel bedding, G123×9, E2: Parallel bedding, G32-30, E3: Ripple cross-bedding, G3×3, E4: Inverse graded, Ripple cross-bedding, G123×9, E5: Ripple cross-bedding, G123×9, E6: Composite bedding, G8×1, E7: Fault plane, Asphaltene, G66×5, F1: Mud, G66×3, F2: Mud, Inverse graded, F3: Mud, G65-1, F4: Mud, G3104, F5: Erosion surface, G5, F6: Erosion surface, G83-10, F7: Erosion surface, G8×1

Code	Lithofacies	Typical example	Code	Lithofacies	Typical example
FcM	Fine-grained conglomerate with massive-bedding		FiM	Fine-grained sandstone with massive-bedding	
FcT	Fine-grained conglomerate with trough cross-bedding		FiT	Fine-grained sandstone with trough cross-bedding	
GI	Glutenite with inverse graded-bedding		FiP	Fine-grained sandstone with parallel-bedding	
GN	Glutenite with normal graded-bedding		FiL	Fine-grained sandstone with low angle cross-bedding	
GcM	Gravel-bearing coarse-grained sandstone with massive-bedding		SI	Sandstone with inverse graded-bedding	
GcT	Gravel-bearing coarse-grained sandstone with trough cross-bedding		SN	Sandstone with normal graded-bedding	
CT	Coarse-grained sandstone with trough cross-bedding		AsR	Argillaceous siltstone with ripple cross-bedding	
MeH	Medium-grained sandstone with high angle cross-bedding		SiW	Siltstone with wave and lenticular-bedding	
MeT	Medium-grained sandstone with trough cross-bedding		SiR	Siltstone with ripple cross-bedding	
MeM	Medium-grained sandstone with massive-bedding		MH	Mud with horizontal-bedding	
GmP	Gravel-bearing medium-grained sandstone with parallel-bedding		MM	Mud with massive-bedding	

Fig. 8 Typical lithofacies of the Shahejie Formation in Nanpu Sag, Bohai Bay Basin

coarse-grained sandstone, fine-grained sandstone, and muddy sandstone mixed with grayish-green and brownish-gray mudstone (Fig. 10d). SQ5 features medium amplitude, sub-parallel seismic reflection package reflection. Its lithology primarily includes pebbly sandstone and coarse- to medium-grained sandstone interbedded with brown-gray mudstone (Fig. 10e). Finally, SQ6 exhibits medium to medium-weak amplitude seismic reflection package reflection with hummocky-shaped and local chaotic reflections. The lithology consists of light-gray, medium- to coarse-grained sandstone and brown-gray mudstone interbedding, with coarse grains in the upper part and finer grains below (Fig. 10f).

The seismic reflection package reflections within the study area are classified into three distinct categories. Type I phase exhibits medium continuity and medium to

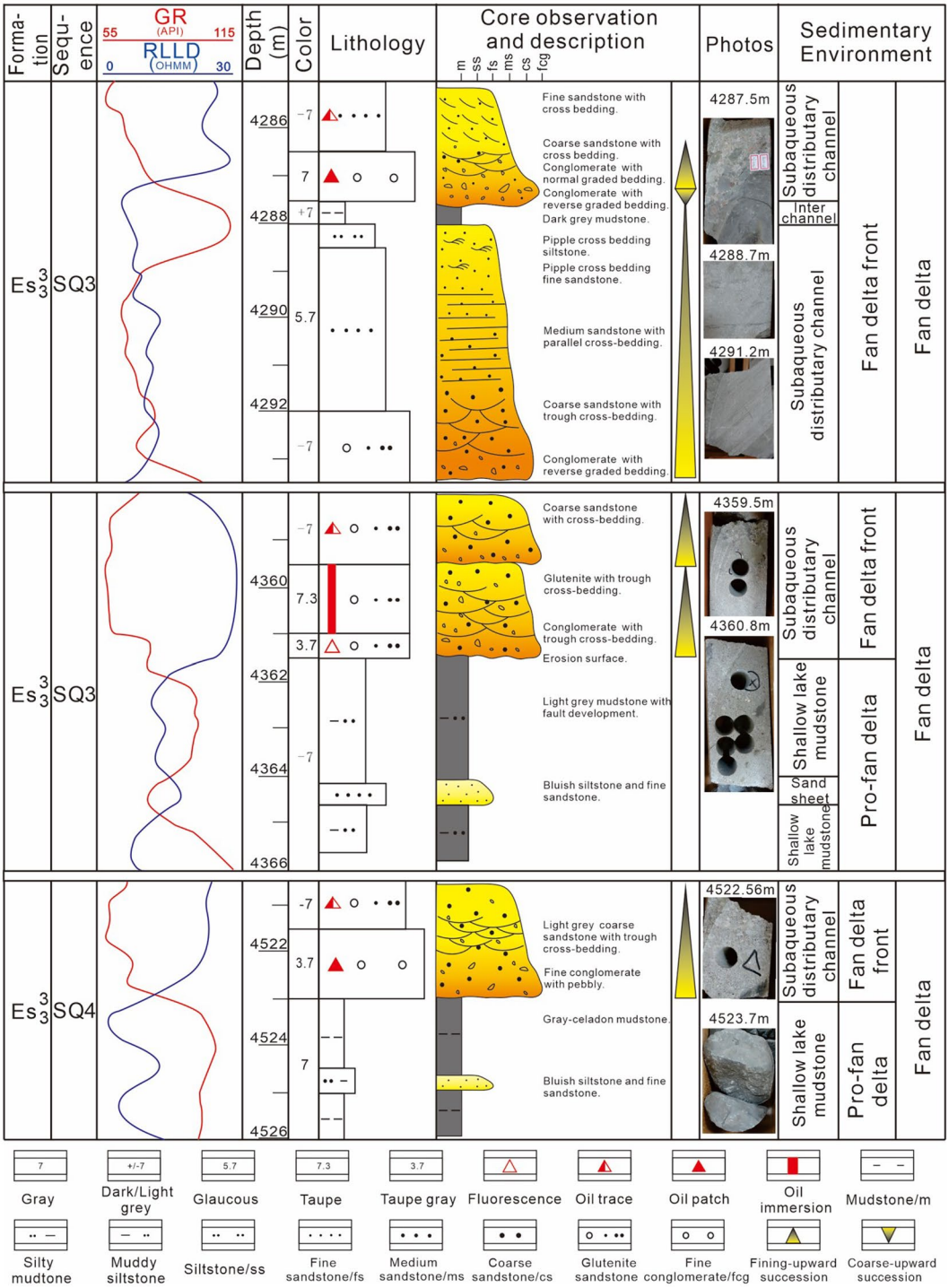

Fig. 9 Single-well sedimentary profile of the Shahejie Formation in Nanpu Sag, Bohai Bay Basin (G66-5)

weak amplitude with parallel to sub-parallel reflections; they typically correspond to the distribution of braided river channels and areas enriched with sand bodies. Type II phase, characterized by strong amplitude and continuous to relatively continuous parallel to sub-parallel reflections, marks the presence of front sand bars. Type III phase, which displays medium to strong amplitude and relatively continuous parallel to sub-parallel reflections, is associated with mudstone-enriched areas, which are indicative of front sand sheet distributions.

Fig. 10 Seismic reflection package reflection distribution characteristics of the Shahejie Formation in Nanpu Sag, Bohai Bay Basin. **a** SQ1; **b** SQ2; **c** SQ3; **d** SQ4; **e** SQ5; **f** SQ6. I: moderate to weak amplitudes, moderate continuous, parallel to sub-parallel and progradational reflection configuration, represents the braided channel and other sand-rich; II: strong amplitude, continuous to relatively continuous, parallel to sub-parallel reflection configuration, represents front sand bar; III: medium to strong amplitude, relatively continuous, parallel to sub-parallel reflection configuration, represents other mud-rich

Discussion

Based on detailed analyses of sequence stratigraphy, core samples, sand body morphology, sedimentary rhythms, seismic reflection characteristics, and sand body distribution patterns, it has been determined that the sediment sources for the study area are the Xinanzhuang and Baigezhuang uplifts. Fan delta deposits predominate within the target strata, leading to enhancements in the key sedimentary patterns (Cullen et al. 2020; Xu et al. 2023b).

Sedimentary environments

The sedimentary environment has been identified as a fan delta, which was derived from a synthesis of the sediment source, lithology types, maturity, lithofacies, sedimentary sequences, and seismic reflection package

reflection analyses. The fan delta has further been subdivided into the fan delta plain, fan delta front, and pro-fan delta zones (Mahata and Maiti 2019; Abdel-Fattah and Sehsah 2023; Qu et al. 2023). Within these zones, distinct features, such as the main channel, braided channel, mid-fan front, mid-fan sand bar, front sand sheet, interfan, overbank, inter-channel, and mud zones, have been delineated (Fig. 11a–f).

Fan delta plain

In the study area, the fan delta plain, situated above sea level near an active fault zone with a steep slope, comprises braided channel and overbank deposits. The climate during the depositional period was characterized as arid to semiarid (Kashif et al. 2020; Wu et al. 2022). The area experienced shallow, channelized flood currents that were intermittent and abrupt. The fan delta plain facie represents the coarsest section of the entire fan body, distinguished by its varied granularity, complex composition, and poor textural attributes such as sorting and roundness. Additionally, it has low compositional maturity, with lithic arkose as the predominant rock type (Cullen et al. 2020). The stratification typically lacks clarity and regularity, with notable large cross-bedding, imbricate structures, and scour-filling structures that display a fining-upward succession.

Fan delta front

The lithology of the fan delta front varies significantly, consisting of conglomerate, glutenite, and sandstone. This area represents the most productive reservoir within the fan delta and it has been categorized into several depositional environments: subaqueous distributary channels, inter-channel channels, mid-fan fronts, front sand bars, and front sand sheet deposits.

(1) Subaqueous distributary channel

The sand body of the subaqueous distributary channel is the predominant type within the fan delta front facies, and it represents a high-quality reservoir in the fan delta sedimentary environment. Formed by forward-extending and bifurcating braided channels, it serves as the conduit for sediment entry into the basin (Nguidi et al. 2021; Abdel-Fattah and Sehsah 2023). Frequent bifurcation and flow diversions led to substantial heterogeneity in the reservoir, both laterally and vertically (Nguidi et al. 2021; Kane et al. 2023). The morphology of the sand body has a zonal distribution along the flow direction on the plane and it is lenticular in the cross-section (Soh et al. 1995; Abdel-Fattah and Sehsah 2023). The sediment thickness values are greatest at the center of the fluvial bed and they taper off toward the sides or front. The channel is characterized by a succession of conglomerate, glutenite, and sandstone with fining-upward cycles. Common sedimentary structures include large trough cross-bedding, planar cross-bedding, low-angle cross-bedding, and inclined bedding from bottom to top. The lithofacies of the subaqueous distributary channel typically include FcM, FcT, GI, GN, GcM, CT, GmP, and MeT, among others. The spontaneous potential (SP) and gamma ray (GR) curves generally exhibit bell or box shapes. The rock types are primarily litharenite, lithic arkose, and feldspathic litharenite, characterized by low compositional and structural maturity, poor sorting, and varied particle sizes. Multiphase channel stacking enhanced the lateral connectivity of the sand body. Core data analyses show that channel porosity typically ranges from 12.9 to 18.6%, with an average permeability of 13.4×10^{-3} μm^2, indicating high porosity and high permeability and thus excellent reservoir potential for oil and gas resources (Zhang et al. 2022). However, it is important to note that faults and structural influences can adversely affect sand body connectivity (Fig. 11g, h).

(2) Inter-channel

The inter-channel is the low place between fluvial channels, and the lithofacies are mainly composed of mudstone, silty mudstone with massive-bedding, silty mudstone with horizontal bedding, and argillaceous siltstone with intercalation of thin sandstone. The rock types are mainly lithic arkose and feldspathic litharenite, the compositional and structural maturity of the sediments are both low, and the sorting and roundness are better, while the detrital particles are fine-grained. Its porosity and permeability are relatively low, and it is often a restraining barrier or interlayer of oil and gas reservoirs (Ichaso et al. 2022; Zhang et al. 2022).

(3) Mid-fan front

Located at the forefront of the subaqueous distributary channel, the mid-fan front represents a zone where the sediments were deposited from weakening, directionally high-energy flows but it maintained high sandstone ratio (Hayward 1985; Ichaso et al. 2022). The lithology of the mid-fan front consists of a fining-upward succession characterized primarily by fine-grained to medium-grained sandstones. The prevalent lithofacies include massive-bedding, parallel-bedding, and normal graded-bedding. The dominant rock types are lithic arkose and feldspathic litharenite, with sediments displaying moderate compositional maturity and moderate to low structural maturity.

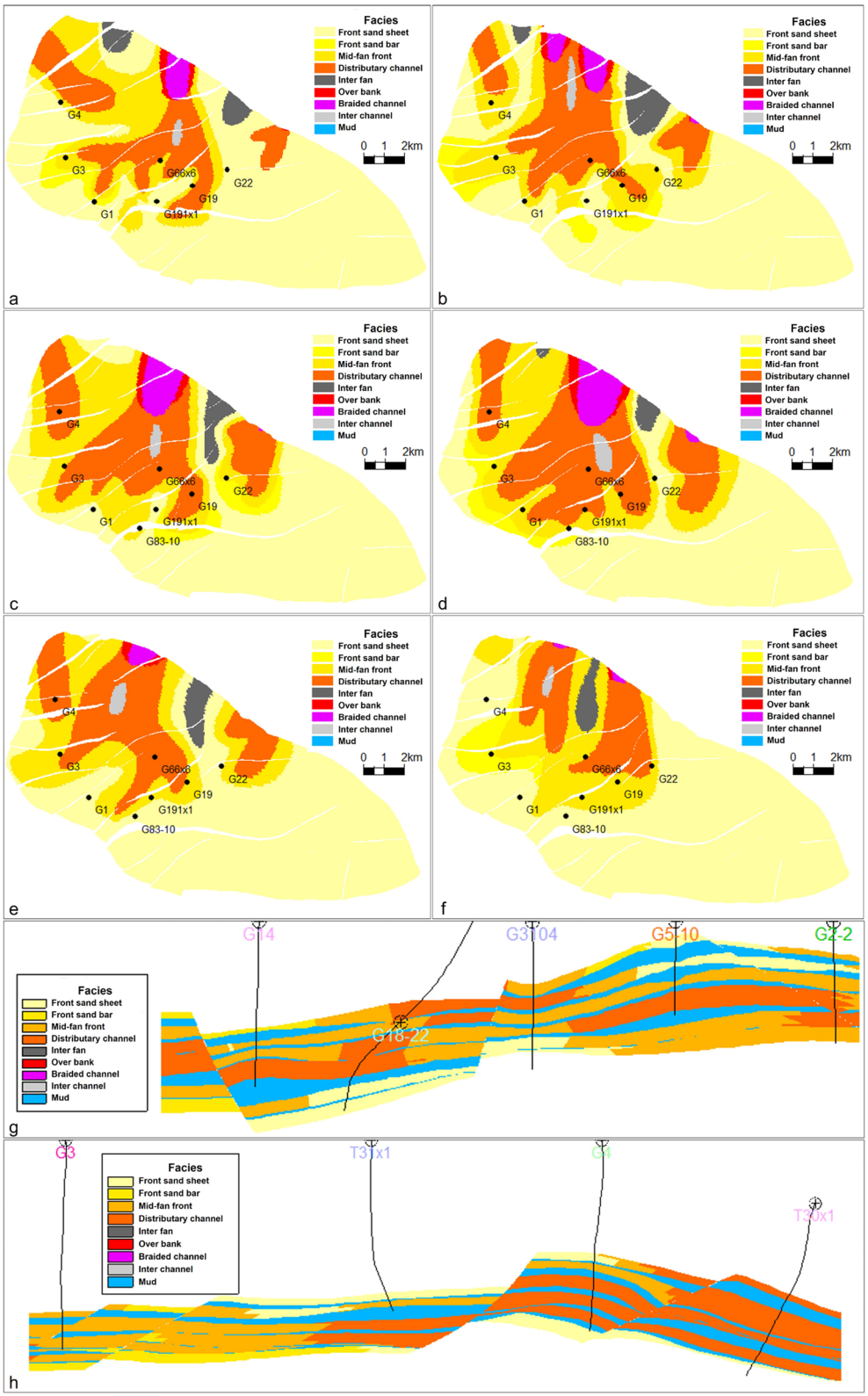

Fig. 11 The distribution characteristics of sedimentary facies in the plane and longitudinal profile of the Shahejie Formation in Nanpu Sag, Bohai Bay Basin. **a** SQ1; **b** SQ2; **c** SQ3; **d** SQ4; **e** SQ5; **f** SQ6; **g** profile B in Fig. 1; **h** profile C in Fig. 1

(4) Front sand bar

Located at the forefront of the subaqueous distributary channel, the front sand bar was formed from the sediments deposited by weakening, directionally high-energy flows. Although its extent and scale are relatively smaller than those of a typical delta mouth bar, it exhibits a high ratio of sandstone to stratum thickness (Hayward 1985; Soh et al. 1995; Ichaso et al. 2022; Abdel-Fattah and Sehsah 2023). The lithology of the front sand bar features a coarsening-upward succession and displays moderate to small sedimentary structures. The dominant lithofacies include fine-grained to medium-grained sandstone characterized by massive-bedding, parallel-bedding, and normal graded-bedding. The primary rock types are lithic arkose and feldspathic litharenite, with sediments showing moderate compositional maturity and moderate to low structural maturity.

(5) Front sand sheet

The front sand sheet marks the terminus of the subaqueous distributary channel. Here, the sediments are characterized by thin layers of fine-grained material. The primary rock types in this region are lithic arkose and feldspathic litharenite, with sediments exhibiting high compositional maturity and moderate structural maturity. During the process of weakening directional low energy flow, the predominant lithofacies include AN, AsR, SiR, and SiW, among others (Soh et al. 1995; Nguidi et al. 2021; Abdel-Fattah and Sehsah 2023; Kane et al. 2023).

Pro-fan delta

The pro-fan delta is characterized by fine-grained siltstone and mudstone, featuring horizontal bedding and biological fossils. The predominant rock types are lithic arkose and feldspathic litharenite, with both the compositional and structural maturity of the sediments being high. Deposits in the pro-fan delta transition into lacustrine argillaceous sediments toward the basin, displaying no distinct boundary.

Sedimentary pattern evolution

The sedimentary pattern elucidates the relationships among sedimentary environments, sedimentation processes, and their genesis, offering theoretical generalizations of sedimentary facies (Armas et al. 2021; Ichaso et al. 2022). This pattern not only captures the quintessential characteristics of sedimentary facies, but also explains the formation processes and mechanisms, reflecting the fundamental connections between sedimentary facies and their environmental contexts (Pondrelli et al. 2011; Kashif et al. 2020; Zhang et al. 2022).

Building on previous research, our study also incorporated sequence factors into the modeling of evolutionary processes. These sequences influence the longitudinal distribution of sediments and are governed by factors such as water level changes, tectonic subsidence, sediment supply, and climate conditions (Carvalho and Schulte 2013; Zhang et al. 2022).

The fan delta sediments in the study area were influenced by lacustrine progression and regression sequences (Fig. 12; Carvalho and Schulte 2013; Kashif et al. 2020; Zhang et al. 2022). Within the Shahejie Formation, the SQ5 and SQ6 of the Es_3^3 sub-member were deposited in lacustrine environments during the retreat period. From SQ6 to SQ5, as the base level rose, the fan delta advanced into the basin, leading to increased sandstone thickness, reduced mudstone layers, and a higher sand–mud ratio, which is indicative of progradation (Fig. 12). This resulted in the sedimentary sequence exhibiting an inverse grain cycle. The scales of the subaqueous distributary channels, mid-fan fronts, front sand bars, and braided channels expanded correspondingly. The log data reveal similar trends, with increases in the low values of the GR (natural gamma) curve and expansions in the box-type and funnel-type curves. Additionally, the scale of the Type I and Type II seismic reflection package reflections expanded, while that of the Type III seismic reflection package reflection narrowed, correlating with the distribution ranges of the braided river channels, front sand bars, and sand body enrichment areas. The seismic sections show deteriorating reflection and continuity from the bottom upward.

In SQ4 of the Es_3^3 sub-member within the Shahejie Formation, the fan delta's spread was extensive, and a well-developed sand body is prominent nearby, marking a base level transition and a longitudinal shift from a progradation sequence to a retrogradation sequence. Notably, the SQ4 vicinity forms the main reservoir, with GR logging curves exhibiting box-type and bell-type characteristics. The seismic section has continuously improved upward reflections and increases in reflection intensity from weak to strong, with extensive development of Type I and Type II seismic reflection package reflections. SQ4 is characterized by fan delta front features, with interchannel and subaqueous distributary channel environments identified in Well G66-5 (Fig. 9; Soh et al. 1995; Zhang et al. 2022; Abdel-Fattah and Sehsah 2023).

During the SQ4 period, scales of the subaqueous distributary channel, mid-fan front, front sand bar, and braided channel were the largest. As the base level decreased from SQ4 to SQ1, the lake level rose, basin accommodation expanded, and the fan body retreated

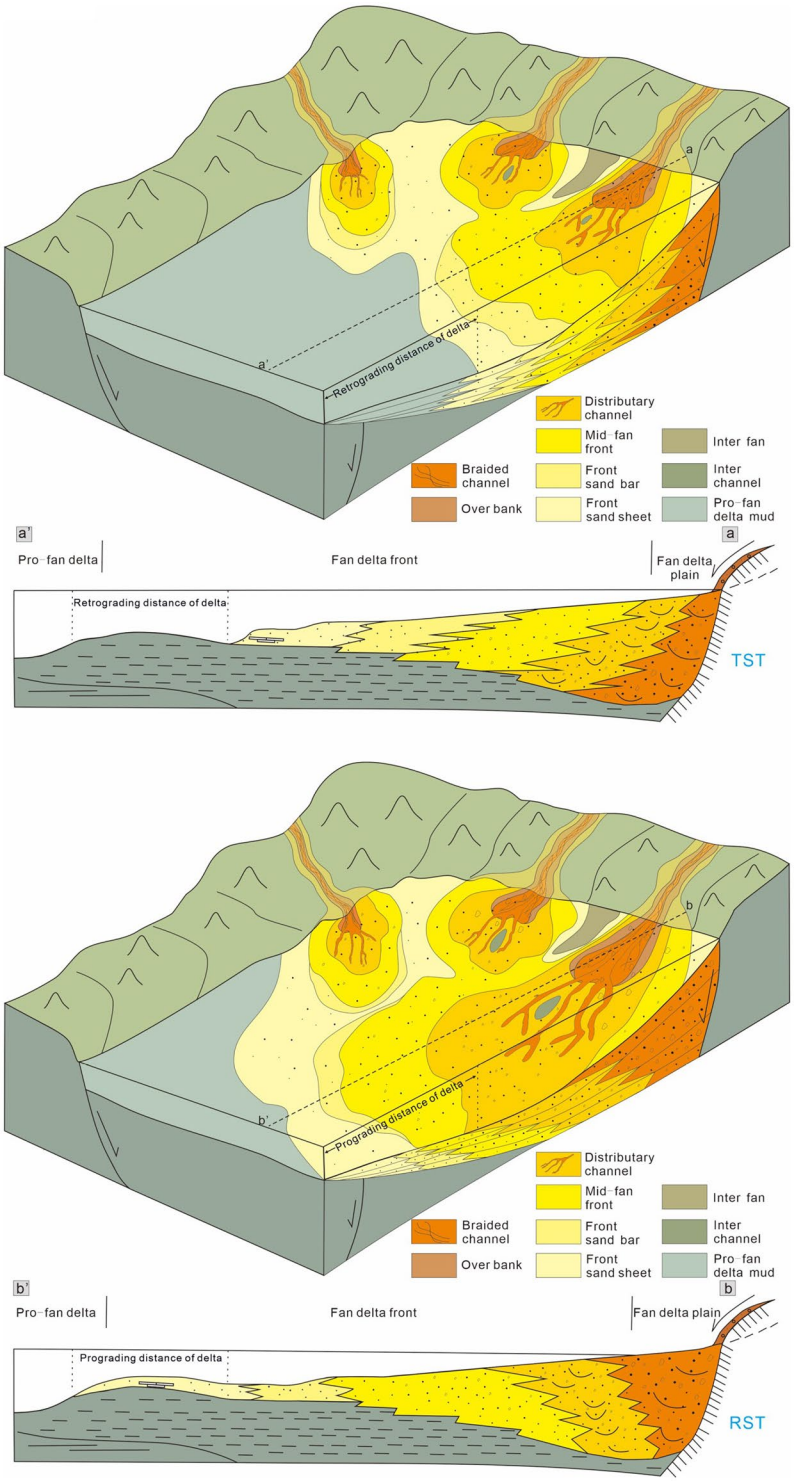

Fig. 12 Sedimentary facies pattern of the Shahejie Formation in Nanpu Sag, Bohai Bay Basin

toward the basin margin, resulting in reductions in the sand layer thickness values (Fig. 12). Consequently, the scales of the Type I and Type II seismic reflection package reflections narrowed, while the Type III seismic reflection package reflection, indicating mudstone-enriched areas, expanded to encompass the front sand sheet distribution

range. SQ3 can be categorized as a pro-fan delta and fan delta front, indicative of a shallow lake with sand sheet, inter-channel, and subaqueous distributary channel environments (Fig. 9; Zhang et al. 2022; Abdel-Fattah and Sehsah 2023; Qu et al. 2023). The scales of the subaqueous distributary channels, mid-fan fronts, front sand bars, and braided channels gradually decreased, while the inter-fan, inter-channel, front sand sheet, and mud presence increased, exhibiting reverse grain cycle characteristics from bottom to top (Fig. 12). SQ1 is marked by the deposition of approximately 100 m of dark mudstone, defining the top boundary of this sequence.

Conclusions

Based on our study, we draw the following conclusions:

(1) The stratigraphic sequence in the Nanpu Sag of the Bohai Bay Basin has six fourth-order sequences, identified as SQ1 to SQ6 within Es_3^{2+3}, featuring both progradation and regressive sequences.
(2) The Xinanzhuang and Baigezhuang Uplifts in the northern area supplied sediments to the sedimentary system of the study area. These sediments consist primarily of lithic arkose and feldspathic litharenite, with an average maturity index of 0.39, indicating low rock maturity in the target formation.
(3) The Nanpu Sag hosts a diverse range of lithofacies, including FcM, FcT, GI, GN, GcM, GcT, CT, MeH, MeT, MeM, GmP, FiM, FiT, FiP, FiL, SI, SN, AsR, SiW, SiR, MH, and MM. These lithofacies and their associations within single-well sedimentary sequences depict a variety of sedimentary processes across multiple sub-environments within the fan delta system. These environments include the fan delta plain braided channel, overbank, inter-fan, front distributary channel, mid-fan front, inter-channel, sand bar, sand sheet, and pro-fan delta mud.
(4) The seismic reflection package reflections of the Nanpu Sag have been classified into three categories having these characteristics: medium continuous, medium to weak amplitude, parallel to sub-parallel seismic reflection package reflection; strong amplitude, continuous to relatively continuous, parallel to sub-parallel seismic reflection package reflection; and medium to strong amplitude, relatively continuous, parallel to sub-parallel seismic reflection package reflection. Each category corresponds to distinct geological features within the basin: braided river channels and sand body enrichment areas, front sand bars, and mudstone enrichment areas, respectively.
(5) The sedimentary environment of the study area is identified as a fan delta, comprising the fan delta plain, fan delta front, and pro-fan delta. Within these segments, features such as the main channel, braided channel, mid-fan front, mid-fan sand bar, front sand sheet, inter-fan, over bank, and inter-channel are further discernible. The sediment dynamics in the fan delta are influenced by lacustrine progression and regression sequences. Notably, during the retreat period, SQ6 to SQ5 exhibited progradational characteristics, marking a significant phase in sedimentary development, during the water level rising period, while SQ4 to SQ1 exhibited retrogradational characteristics.

Acknowledgements
The authors acknowledge the Jidong branch of PetroChina Company Limited's invaluable assistance in core observation and sample collection.

Author contributions
Sun ZQ, Lin SY, and Wang MQ performed the data collection and analysis. Sun ZQ, Liu LL, and Wang GQ contributed to the interpretation of the results and the preparation of the manuscript. All authors read and approved the final manuscript.

Funding
This study is supported by the Ocean Young Talent Innovation Project of Zhanjiang (Study on the influence of sediment-coastal current system on mangrove growth environment in the Leizhou Peninsula under multiple environmental factors, no. 2022E05012), the Special Talents Funding Project of Lingnan Normal University (Study on fluvial reservoir architecture characterization and 3D geological modeling, no. ZL2021012), the general project of Lingnan Normal University (Study on the sedimentary morphology and forming environment of coastal dune in the Donghai Island, Zhanjiang, no. LY2210), the Young Innovative Talents Program of Universities in Guangdong Province (Study on the sedimentary environment of mangrove wetland in Zhanjiang Bay based on sediment element-mineral-grain size, no. 2022KQNCX045), and the Teaching Quality and Teaching Reform Project of Lingnan Normal University (2022-Introduction to Earth Sciences), and the Quality General Studies program of Lingnan Normal University (2023-Modern Physical Geography).

Availability of data and materials
The datasets used and/or analyzed during the current study are available from the corresponding author on reasonable request.

Declarations

Competing interests
All authors declare that there are no competing interests.

Received: 21 November 2023 Accepted: 7 June 2024
Published online: 21 June 2024

References

Abdel-Fattah ZA, Sehsah H (2023) The Upper Neoproterozoic lacustrine–fan delta depositional systems associated with braided alluvial fans in the Nubian Shield, Egypt. Sediment Geol 452:106426
Allen JP, Fielding CR (2007a) Sedimentology and stratigraphic architecture of the Late Permian Betts Creek Beds, Queensland, Australia. Sed Geol 202:5–34

Allen JP, Fielding CR (2007b) Sequence architecture within a low-accommodation setting: an example from the Permian of the Galilee and Bowen basins, Queensland, Australia. AAPG Bull 91(11):1503–1539
Armas P, Cristofolini E, Escribano F, Camilletti G, Barzola M, Otamendi J, Cisterna C, Leisen M, Romero R, Barra F, Tibaldi A (2021) Lower-middle Ordovician sedimentary environment and provenance of the Suri formation in the northern region of the Famatina belt, Catamarca, Argentina. J S Am Earth Sci 105:102948
Boggs S (2011) Principles of sedimentology and stratigraphy, 5th edn. Pearson Education, New Jersey
Carvalho F, Schulte L (2013) Morphological control on sedimentation rates and patterns of delta floodplains in the Swiss Alps. Geomorphology 198:163–176
Catuneanu O (2006) Principles of sequence stratigraphy. Elsevier, Amsterdam
Cukur D, Krastel S, Tomonaga Y, Schmincke H-U, Sumita M, Meydan AF, Çağatay MN, Toker M, Kim S-P, Kong G-S, Horozal S (2017) Structural characteristics of the Lake Van Basin, eastern Turkey, from high-resolution seismic reflection profiles and multibeam echosounder data: geologic and tectonic implications. Int J Earth Sci 106:239–253
Cullen TM, Collier REL, Gawthorpe RL, Hodgson DM, Barrett BJ (2020) Axial and transverse deep-water sediment supply to syn-rift fault terraces: insights from the West Xylokastro Fault Block, Gulf of Corinth, Greece. Basin Res 32:1105–1139
Feng CJ, Yao XZ, Yang HZ, Li DM, Sun MS (2021) Source-sink system and sedimentary model of progradational fan delta controlled by restricted ancient gully: an example in the Enping Formation in the Southern Baiyun Sag, Pearl River Mouth Basin, Northern South China Sea. Acta Geol Sin 95:232–247
Haq BU, Schutter SR (2008) A chronology of Paleozoic sea-level changes. Science 322(5898):64–68
Hayward AB (1985) Coastal alluvial fans (fan deltas) of the Gulf of Aqaba (Gulf of Eilat), Red Sea. Sediment Geol 43(1–4):241–260
Hunt D, Tucker ME (1992) Stranded parasequences and the forced regressive wedge systems tract: deposition during base-level'fall. Sed Geol 81(1/2):1–9
Ichaso A, Buatois LA, Mángano MG, Thomas P, Marion D (2022) Assessing the expansion of the Cambrian Agronomic Revolution into fan-delta environments. Sci Rep 12:14431
Jia HB, Ji HC, Lu CJ, Chen L, Yang X, Sun SM, Zhang H (2018) Sequence stratigraphy and depositional system analysis in Paleogene Nanpu Sag: sequence model and sediment partition. Geol J 53(4):1557–1572
Kalifi A, Sorrel P, Leloup P-H, Spina V, Huet B, Galy A, Rubino J-L, Pittet B (2020) Changes in hydrodynamic process dominance (wave, tide or river) in foreland sequences: the subalpine Miocene Molasse revisited (France). Sedimentology 67:2455–2501
Kane OI, Hu MY, Cai QS, Deng QJ, Yang WJ, Zuo MT (2023) Sedimentary facies, lithofacies paleogeography, and an evaluation of the Ordovician sequences in the Sichuan Basin, southwest China. Mar Pet Geol 149:106096
Kang X, Hu WX, Cao J, Wu HG, Xiang BL, Wang J (2019) Controls on reservoir quality in fan-deltaic conglomerates: insight from the Lower Triassic Baikouquan Formation, Junggar Basin, China. Mar Pet Geol 103:55–75
Kashif M, Cao YC, Yuan GH, Asif M, Rehman F, Shehzad K, Ullah MF, Mustafa G (2020) Sedimentology of Shahejie Formation, Bohai Bay Basin: a case study of Es1 member in Nanpu Sag. Carbonates Evaporites 35(2):1–18
Knapp LJ, Harris NB, McMillan JM (2019) A sequence stratigraphic model for the organic-rich Upper Devonian Duvernay Formation, Alberta, Canada. Sed Geol 387:152–181
Kra KL, Qiu LW, Yang YQ, Yang BL, Ahmed KS, Camara M, Kouame EM (2022) Depositional and diagenetic control on conglomerate reservoirs: an example from the fourth member of shahejie formation in the Lijin Sag, Bohai Bay Basin, east China. J Petrol Sci Eng 218:110913
Li JZ, Zhang JL, Sun SY, Zhang K, Du DX, Sun ZQ, Wang YY, Liu LL, Wang GQ (2018) Sedimentology and mechanism of a lacustrine syn-rift fan delta system: a case study of the Paleogene Gaobei Slope Belt, Bohai Bay Basin, China. Mar Pet Geol 98:477–490
Li SM, Ji H, Wan ZH, Pang XQ, Zhang HG, Xu TW, Zhou YS (2021) Geochemical characteristics and factors controlling the deep lithologic reservoirs in Puwei Sag, Dongpu Depression-a case study of well PS20. J Petrol Sci Eng 203:108669
Liu QH, Zhu XM, Yang Y, Geng MY, Tan MX, Jiang L, Chen L (2016) Sequence stratigraphy and seismic geomorphology application of facies architecture and sediment-dispersal patterns analysis in the third member of Eocene Shahejie Formation, slope system of Zhanhua Sag, Bohai Bay Basin, China. Mar Pet Geol 78:766–784
Liu QH, Zhu XM, Zeng HL, Li SL (2019) Source-to-sink analysis in an Eocene rifted lacustrine basin margin of western Shaleitian Uplift area, offshore Bohai Bay Basin, eastern China. Mar Pet Geol 107:351–364
Liu ET, Wang H, Feng YX, Pan SQ, Jing ZH, Ma QL, Gan HJ, Zhao JX (2020) Sedimentary architecture and provenance analysis of a sublacustrine fan system in a half-graben rift depression of the South China Sea. Sed Geol 409:105781
Liu HQ, Jin PB, Liu JD, Liu H, Zou J, Chen L (2023) Characteristic of faults and its control on hydrocarbon accumulation in Laoyemiao structural belt, Nanpu Depression. Geol China 1:1–13
Mahata HK, Maiti R (2019) Evolution of Damodar fan delta in the western Bengal Basin, west Bengal. J Geol Soc India 93:645–656
Makled WA, Mandur MMM, Langer MR (2017) Neogene sequence stratigraphic architecture of the Nile Delta, Egypt: a micropaleontological perspective. Mar Pet Geol 85:117–135
Miller KG, Kominz MA, Browning JV, Wright JD, Mountain GS, Katz ME, Sugarman PJ, Cramer BS, Christie-Blick N, Pekar SF (2005) The Phanerozoic record of global sea-level change. Science 310(5752):1293–1298
Moore KR, Pajusalu M, Gong J, Sojo V, Matreux T, Braun D, Bosak T (2020) Biologically mediated silicification of marine cyanobacteria and implications for the Proterozoic fossil record. Geology 48:862–866
Moran MG, Holbrook J, Lensky NG, Moshe LB, Mor Z, Eyal H, Enzel Y (2023) Century-scale sequences and density-flow deltas of the late Holocene and modern Dead Sea coast, Israel. Sedimentology 70:1945–1980
Nguidi MA, Mouflih M, Benbouziane A, Kocsis L, Ouariti SE, Boukhari HE, Aquit M, Yazami OK (2021) Lithofacies analysis, sedimentary dynamics and genesis of Maastrichtian-Eocene phosphorites of BouCraa deposit (Southern Morocco). J Afr Earth Sc 177:104161
Pang H, Huo XG, Pang XQ, Liu GY, Ma Q, Bai H, Wang JW, Zhang YC, Huang SM, Wu S, Zhang XG (2023) Quantitative characterization of critical reservoir physical properties of tight oil charging in the third member of the Shahejie Formation in the Gaobei Slope of Nanpu Sag, Bohai Bay Basin. Geoenergy Sci Eng 230:212212
Peter MB (2016) RESEARCH FOCUS: the future of the sequence stratigraphy paradigm: dealing with a variable third dimension. Geology 44(4):335–336
Pondrelli M, Rossi AP, Platz T, Ivanov A, Marinangeli L, Baliva A (2011) Geological, geomorphological, facies and allostratigraphic maps of the Eberswalde fan delta. Planet Space Sci 59(11–12):1166–1178
Prather BE, Falivene O, Burgess PM (2022) Stratigraphic analysis of XES02: Implications for the sequence stratigraphic paradigm. J Sediment Res 92(10):934–954
Qu YQ, Pan JG, Yin L, Xu DN, Teng TY, Wang GD (2023) Identification of favorable underwater reservoirs in a conglomerate fan delta. Geoenergy Sci Eng 221:111307
Rohais S, Eschard R, Guillocheau F (2008) Depositional model and stratigraphic architecture of rift climax Gilbert-type fan deltas (Gulf of Corinth, Greece). Sed Geol 210(3–4):132–145
Soh W, Tanaka T, Taira A (1995) Geomorphology and sedimentary processes of a modern slope-type fan delta (Fujikawa fan delta), suruga trough, Japan. Sediment Geol 98(1–4):79–95
Sun PK, Jia LB, Zhu HZ, Zhang L, He TH, Xu ZH, Li C (2021) Sequence architecture and sedimentary filling characteristics of the middle-upper part of the Es3 Formation in the Liuzan Area, Nanpu Depression. Pet Sci Bull 1:16–30
Sun ZQ, Chen ZH, Liu LL, Li Y, Zhang JL, Shen WL (2023a) How to distinguish between marine and lacustrine sedimentary environments?—a case study of Lishui Sag, East China Sea Shelf Basin. Geoenergy Sci Eng 228:212032
Sun YH, Liu L, Meng LJ, Ma Y (2023b) Characteristics of brush structures in No. 1 structural belt and their geological significance in Nanpu Sag. Oil Geophys Prospect 58(4):983–992
Talarico ECS, Grana D, Figueiredo LP, Pesco S (2020) Uncertainty quantification in seismic phase inversion. Geophysics 85:43–56
Tang L, Song Y, Pang XQ, Jiang ZX, Guo YC, Zhang HA, Pan ZH, Jiang H (2019) Effects of paleo sedimentary environment in saline lacustrine basin on

organic matter accumulation and preservation: a case study from the Dongpu Depression, Bohai Bay Basin, China. J Pet Sci Eng 185:106669
Wrona T, Pan I, Gawthorpe RL, Fossen H (2018) Seismic phase analysis using machine learning. Geophysics 83:83–95
Wu H, Ji YL, Du ZW, Zhou Y, Zou J, Zhang YZ, Du W, Liu HQ (2022) Evolution and controls of high reservoir quality in Oligocene sandstones from moderate to deep burial, Nanpu Sag, Bohai Bay Basin, China. Sediment Geol 441:106275
Xu W, Fan TE, Song LM, Chen KY (2023a) Sedimentary process of channel-feeding fan delta in the south of Albert Rift, Uganda: insight from sensitivity analysis of forward stratigraphic modeling. Mar Pet Geol 155:106375
Xu TY, Bai YZ, Yang G, Fang XS, Liu YG, Tao CF, Shi XF (2023b) Seismic reflection characteristics and controlling factors of shallow gas in the alongshore mud clinoform of the East China Sea. Mar Pet Geol 158(Part B):106570
Yang T, Cao YC, Wang YZ, Cai LX, Liu HN, Jin JH (2023) Sedimentary characteristics and depositional model of hyperpycnites in the gentle slope of a lacustrine rift basin: a case study from the third member of the Eocene Shahejie Formation, Bonan Sag, Bohai Bay Basin, Eastern China. Basin Res 35:1590–1618
Yao SQ, Gomez-Rivas E, Martín-Martín JD, Gómez-Gras D, Travé A, Griera A, Howell JA (2020) Fault-controlled dolostone geometries in a transgressive–regressive sequence stratigraphic framework. Sedimentology 67(6):3290–3316
Zhang K, Wu SH, Wang JJ, Xu YJ, Xu ZH, Zhang JJ (2022) Vertical grain-size trend of mouth bar in lacustrine fan delta: flume experiments. Pet Sci 19(5):1964–1977
Zou J, Liu GY, Ma Q, Yu FS, Meng LJ, Tian B (2023) Analysis of fault characteristics and oil and gas enrichment differences in the No. 2 structural belt, Nanpu Sag, Bohai Bay Basin, East China. Front Earth Sci 10:1057660

Publisher's Note